3-D MHD Simulations of the Interaction of Magnetic Flux Tubes

D. Kondrashov, J. Feynman, P. C. Liewer, A. Ruzmaikin, Jet Propulsion Laboratory, California Institute of Technology, Pasadena, CA 91109

Received ______________________; accepted ______________________

ABSTRACT

We use a 3-D Cartesian resistive MHD code to investigate 3-D aspects of the interaction of magnetic flux tubes as observed in the solar atmosphere and studied in laboratory experiments. We present here the first results from modeling the reconnection of two Gold-Hoyle magnetic flux tubes which follow the system evolution to a final steady state. The energy evolution and reconnection rate for flux tubes with both parallel and antiparallel axial fields and with equal and nonequal strengths are studied. For the first time, we calculate a gauge-invariant relative magnetic helicity of the system and compare its evolution for all the above cases. We observed that the rate at which helicity is dissipated may vary significantly for different cases, and it may be comparable with the energy dissipation rate. The footpoints of the interacting flux tubes were held fixed or allowed to move to simulate different conditions in the solar photosphere. The cases with fixed footpoints had lower magnetic energy release and reached a steady state faster than cases with moving footpoints. For all computed cases the magnetic energy was released mostly through work done on the plasma by the electromagnetic forces rather than through resistive dissipation. The reconnection rate of poloidal magnetic field is faster for the case with antiparallel flux tubes than for the case with parallel flux tubes, consistent with laboratory experiments. We find that during reconnection supersonic (but subalfvenic) flows develop, and it may take a considerably longer time for the system to reach a steady state than for magnetic flux to reconnect. It is necessary to retain the pressure gradient in the momentum equation; the plasma pressure may be significant for the final equilibrium steady state even with low-beta initial conditions.

1. Introduction

The interaction of **magnetic flux tubes** as a source of activity is widely discussed in astrophysics. Solar phenomena such as **coronal mass ejections** and **solar flares,** which are responsible for sudden release of energy into the solar corona and the solar wind, are associated with **magnetic loop interactions** in the solar atmosphere. **Magnetic reconnection** is an important part of this interaction.

Magnetic reconnection changes the configuration of the magnetic field and allows the release of magnetic energy into kinetic and thermal energy of the plasma. It is generally accepted that magnetic reconnection can be studied with **resistive magnetohydrodynamic** (MHD) models and it has been extensively studied using 2-D MHD models. However, real magnetic field configurations in solar and astrophysical plasmas have complex 3-D topologies. Much of the magnetic field of the solar corona is in the form of magnetic flux tubes with **twisted field lines** (Canfield et al. 1996; Rust & Kumar 1994). Frequent transient X-ray brightenings in solar active regions have been linked to local plasma heating due to the interaction of magnetic loops (Shimizu et al. 1994). *Yohkoh* soft X-ray observations provided evidence of magnetic reconnection in the quiet corona resulting in a large scale rearrangement of magnetic structures and significant heating of the plasma (Tsuneta 1996). Recent laboratory experiments (Yamada et al. 1997) have provided evidence of some important 3-D features of magnetic reconnection. In particular, the reconnection rate and the final field configuration are to a large extent dependent on the initial configuration of the magnetic field, i.e., whether flux tubes have the same or opposite helicities.

Numerical models represent a valuable tool in understanding 3-D magnetic reconnection effects, complementing experimental studies. Recently, several important 3-D MHD numerical studies of magnetic reconnection between flux tubes have been performed. Dahlburg & Antiochos (1995) performed a 3-D numerical simulation of the reconnection of antiparallel flux tubes with only an axial component of the magnetic field (no twist). They observed that, after the reconnection, the original two flux tubes had divided into four flux tubes. Fushiki & Sakai (1995) used a simplified analytical model of a coronal flux tube, the Gold-Hoyle (1960) solution, in which loop curvature is neglected, but twist is retained. They investigated plasmoid generation during the reconnection of two Gold-Hoyle flux tubes immersed in a plasma of uniform pressure and density and identified complete and partial reconnection, depending on whether the axial magnetic field components of two tubes are parallel or anti-parallel. Lau & Finn (1996) used a 3-D MHD model to analyze topological changes in the field lines in reconnection between either parallel or antiparallel flux tubes created from an initially potential field by twisting the loop footpoints. Ozaki & Sato (1997) used an incompressible 3-D MHD code to study the reconnection of magnetic loops and arcades created by twisting the footpoints of potential field arcades.

We present here our results from 3-D resistive MHD modeling of the interaction of two Gold-Hoyle magnetic flux tubes in a low beta uniform plasma. The purpose of our studies is to expand existing work on 3-D reconnection to capture both the dynamics of the interaction and the final steady-state solution. We use a comprehensive 3-D MHD code MAP3 (Kondrashov & Keefer 1997) and do not make simplifications adopted in the previous studies on magnetic reconnection in the solar corona. In Ozaki and Sato (1997), the plasma pressure gradient in the momentum equation and compressibility effects were neglected. Lau & Finn (1996) retained compressibility, but neglected the pressure gradient. Both effects were found to be important in the present studies. We analyze magnetic field configurations resulting from the reconnection of flux tubes with either parallel or antiparallel axial fields and with equal absolute field magnitudes. Such cases were studied experimentally and were identified as either cohelicity or counterhelicity reconnection (Yamada et al. 1997). We also investigate a case with nonequal magnitudes (10% difference) of antiparallel flux tubes, for which no published experimental results have been reported.

Computational solutions are obtained with two sets of the boundary conditions: a) moving footpoints of the flux tubes, for which reconnection can take place along all the axial length, and b) fixed footpoints, when reconnection takes place in the vicinity of the midplane of the computational domain. In general the cases with fixed footpoints had lower magnetic energy release and reached a steady state faster than cases with moving footpoints. For all computed cases the magnetic energy was released mostly through work done on the plasma by the electromagnetic forces rather than through resistive dissipation.

The cohelicity case involves reconnection and merging of flux tubes with the same sign of twist. One question is whether the twist of the initial flux tubes will add to produce a flux tube with the twist exceeding the limit of the kink instability. Observational studies of coronal structures provided some evidence for such phenomenon (Pevtsov & Canfield 1996). We find that with moving footpoints the two flux tubes merge into one flux tube which has less twist and is more stable. Our calculations show that strong supersonic (though subalfvenic) flows develop during reconnection which prolong the system transition to a steady state. The pressure gradient in the momentum equation can be important for final equilibrium even for the low-beta initial conditions and it is necessary to retain it in the model. For the equal strength counterhelicity case, the final magnetic configuration has no axial field, i.e., the pressure of poloidal magnetic field is balanced by the high beta plasma pressure within the tube. Thus a low-beta initial configuration has transformed to high-beta configuration.

We performed computational tests to investigate the influence of numerical resistivity, and chose a grid for which the resistivity is dominated by its value specified in the code, and not by the numerical resistivity. We verified the code on test simulations of the stability of Gold-Hoyle flux tubes and obtained satisfactory agreement with previous numerical studies (Mikic et al. 1990).

We obtain qualitative agreement with experimental results by Yamada et al. (1997) on 3-D effects of magnetic reconnection. We observed that reconnection proceeds faster in the counterhelicity case than in cohelicity merging, consistent with the laboratory experiments. The reconnection rates of poloidal magnetic field are in the range between rates predicted by Sweet-Parker and Petschek models.

For the first time we calculate a gauge invariant relative magnetic helicity (Berger & Field 1984; Finn & Antonsen 1985) of the two interacting flux tubes and compare its evolution for all computed cases. We observed that the dissipation rate of helicity may vary significantly for different computational cases, and it may be comparable with the energy dissipation rate.

2. Numerical Model

2.1. Governing Equations

We modeled the plasma as a continuous compressible magnetized fluid with mass density ρ, velocity $\mathbf{v}$ and specific internal energy e. Equations governing plasma motion in the Navier-Stokes formulation include the electromagnetic force $\mathbf{J} \times \mathbf{B}$ and $\mathbf{J} \cdot \mathbf{E}$:

$$\frac{\partial \rho}{\partial t} + \nabla \cdot \rho \mathbf{v} = 0, \tag{1}$$

$$\frac{\partial \rho \mathbf{v}}{\partial t} + \nabla \cdot \rho \mathbf{v}\mathbf{v} = \mathbf{J} \times \mathbf{B} - \nabla \mathbf{p}, \tag{2}$$

$$\frac{\partial}{\partial t}(\rho e + \frac{\rho \mathbf{v}^2}{2}) + \nabla \cdot (\rho \mathbf{v}(\frac{\rho \mathbf{v}^2}{2} + \frac{p}{\rho} + e)) = \mathbf{J} \cdot \mathbf{E} \tag{3}$$

The pressure is calculated from the ideal equation of state with a specific heat ratio γ:

$$p = \rho(\gamma - 1)e.$$

We use a Cartesian 3-D MHD code, MAP3 (Kondrashov & Keefer 1997), to compute magnetic field and plasma evolution. MAP3 is a compressible code and the term ∇p in the momentum equation is retained. MAP3 employs a finite-volume technique to obtain a conservative numerical scheme. Plasma flow equations Eq.(1-3) are advanced in time by an explicit algorithm based on the 2nd-order Van Leer scheme.

Unlike most 3-D MHD codes, MAP3 uses the magnetic vector potential **A** to represent the magnetic field **B** and electric field **E**:

$$\mathbf{E} = -\frac{\partial \mathbf{A}}{\partial t}, \quad \mathbf{B} = \nabla \times \mathbf{A}. \tag{4}$$

In this formulation the divergence condition $\nabla \cdot \mathbf{B} = 0$ is always satisfied, which is important for obtaining a physically correct solution. This choice of variables is a major advantage of MAP3 over other 3-D MHD codes which employ the magnetic field as a primitive variable. In these codes, special complex computational procedures are required to meet the $\nabla \cdot \mathbf{B} = 0$ constraint. Electromagnetic variables in MAP3 are defined on a staggered grid, for which the condition $\nabla \cdot \mathbf{B} = 0$ holds with computer precision. Such a layout results in a conservative numerical scheme of 2nd order spatial accuracy. Using the simplest form of Ohm's law, the magnetic vector potential evolution in the code is described by the following equation

$$\frac{\partial \mathbf{A}}{\partial t} - \mathbf{v} \times \mathbf{B} = \frac{\eta}{\mu_0} \nabla \times \nabla \times \mathbf{A} \tag{5}$$

where η is the electrical resistivity, and μ_0 is the vacuum magnetic permeabiliy. The $\mathbf{v} \times \mathbf{B}$ term describes the convection, and the term $(\eta/\mu_0)\nabla \times \nabla \times \mathbf{A}$ describes the diffusion. Both terms are calculated explicitly on a staggered grid. The magnetic Reynolds number is the ratio of the convection term to the diffusion term. It is also called the Lundquist number S, when based on the Alfven speed V_A:

$$S = \frac{L V_A \mu_0}{\eta}.$$

Our computational tests show that for the grids and range of values of S we are using, the resistivity in the code is dominated by the input physical value, and not the numerical resistivity. These computational tests are described in the Appendix. Also included in the Appendix are results of test simulations of the stability of Gold-Hoyle flux tubes used for code verification.

2.2. Initial Conditions

For our initial conditions we use the Gold-Hoyle model for magnetic flux tubes, which represents a solution for a force-free equilibrium flux tube in a simplified geometry (Gold & Hoyle 1960). In this model curvature of the coronal loop is neglected, but the twist of the field lines is retained. The field components can be specified in a cylindrical coordinate system as a free parameter solution:

$$B_z = \pm \frac{B_0}{1 + \frac{r^2}{b^2}}, \quad B_\theta = \frac{rB_0}{b(1 + \frac{r^2}{b^2})}, \quad B_r = 0. \tag{6}$$

The solution for the magnetic vector potential of the Gold-Hoyle field is

$$A_z = -\frac{bB_0}{2} \ln(1 + \frac{r^2}{b^2}), \quad A_\theta = \pm \frac{b^2 B_0}{2r} \ln(1 + \frac{r^2}{b^2}), \quad A_r = 0 \tag{7}$$

The free parameter b represents a flux tube "width". There is a non-zero electrical current associated with a Gold-Hoyle solution and it has the property that the twist angle Φ of the field line is independent of z and radius r:

$$\Phi = \frac{L_z B_\theta}{rB_z} = \frac{L_z}{b} \tag{8}$$

The flux tube with tied footpoints is kink unstable when $\Phi \geq 2.49\pi$ (Hood and Priest, 1981). We have normalized the fundamental variables: the magnetic field by the value B_0, the density by the value of ρ_0, the pressure by the value of $\rho_0 V_A^2/2$, the velocity by the value of V_A, the time by the value of $\tau_A = b/V_A$, the spatial coordinates by the value of b.

The computational domain is a box of the size $L_x = L_y = 20$; $L_z = 2.5\pi$ in normalized units. We initialize the computation by placing two Gold-Hoyle flux tubes parallel to the z-axis with the tube centers located at $x_1 = 7$, $y_1 = 10$ and $x_2 = 13$, $y_2 = 10$ respectively. The initial vector potential **A** and the magnetic **B** fields are computed as the sum of representative fields of individual flux tubes derived from Eq. (6-7): $\mathbf{B} = \mathbf{B_1} + \mathbf{B_2}$, $\mathbf{A} = \mathbf{A_1} + \mathbf{A_2}$. By changing the sign for B_z in Eq. (6) for one of the tubes, we can specify either parallel or antiparallel flux tubes. However the axial electrical currents will be parallel in all cases, so the flux tubes will attract. By changing value of B_0 in Eq.(6) we control the strength of the flux tube.

We compute the interaction of two Gold-Hoyle flux tubes in three cases. The first case is equal parallel flux tubes (cohelicity) - when B_0 has the same value and B_z has the same sign for both flux tubes. The second case is antiparallel equal flux tubes (counterhelicity) - when B_0 has the same absolute value for both flux tubes but B_z has an opposite sign for one of the tubes. The third case is nonequal antiparallel flux tubes - when B_0 has 10% difference in the absolute value and B_z has an opposite sign for one of the tubes. For all three cases we investigated two sets of boundary conditions, which correspond to fixed or moving footpoints, as described below. The flux tubes are immersed in a plasma with uniform pressure and density. We set $\beta = 0.06$, and the electrical resistivity is defined by the dimensionless value $S = bV_A/\eta = 10^3$.

2.3. Boundary Conditions and Computational Grid

For our simplified Gold-Hoyle flux tubes, the curvature of the two loops is neglected and the top and bottom boundaries ($z = 0, L_z$) represent pieces of the solar photosphere surface. At these boundaries no mass flux is allowed, i.e. $V_z = 0$. Footpoints of the flux tubes can be fixed or allowed to move along the top and bottom boundaries. These two cases reflect two different physical conditions of the photospheric plasma. The flux tubes can be brought together by the convective motion of the photospheric plasma; this corresponds to the moving footpoints case in our model. With no convective motion, we have the case of fixed footpoints frozen into the dense photospheric plasma. In the case of fixed footpoints, the reconnection between the flux tubes takes place only in the vicinity of the mid z-plane. With moving footpoints reconnection takes place along the whole axial length.

To study these two cases different boundary conditions are used for tangential components V_τ and A_τ on the top and bottom boundaries. Fixed footpoints are obtained by imposing a perfectly conducting boundary condition

$$E_\tau = -\frac{\partial A_\tau}{\partial t} = 0, \;\; V_\tau = 0.$$

The boundary conditions for moving footpoints are

$$\frac{\partial B_z}{\partial z} = \frac{\partial A_\tau}{\partial z} = \frac{\partial V_\tau}{\partial z} = 0.$$

On the side boundaries we impose perfectly conducting boundary conditions for the electromagnetic field and a no mass flux condition for the plasma flow ($V_n = 0$) for all cases. Three computational grids have been used: fine - 350x350x20, medium - 200x200x20 and coarse - 100x100x20. Uniform grid spacing has been used for all runs because we find that fine-scale phenomena may occur anywhere within the computational domain.

2.4. Magnetic Helicity

Magnetic helicity, which characterizes the twist of magnetic lines in a flux tube, the writhe (kink) of its axis and/or links between different flux tubes, is one of the most interesting and important features of the 3-D interaction. However the usual form of the magnetic helicity $\int \mathbf{A} \cdot \mathbf{B} dV$ is not useful for studying the interaction of flux tubes in the solar atmosphere. This form is gauge invariant only if $B_n = 0$ on all surfaces surrounding the flux system (for example closed flux tubes). This condition is obviously not valid for magnetic loops with footpoints on the photosphere. To overcome this difficulty, Berger & Field (1984) introduced a gauge invariant concept of magnetic helicity of a given configuration which is defined relative to a reference (potential) field.

We investigate the evolution of the relative magnetic helicity using a compact form suggested by Finn & Antonsen (1985):

$$H = \int (\mathbf{A} + \mathbf{A^p})(\mathbf{B} - \mathbf{B^p})dV, \tag{9}$$

where $\mathbf{A}^p$, $\mathbf{B}^p$ define a potential (current-free) field with known B_n^p on the boundaries of the computational domain. The reference field makes the helicity gauge invariant. The equation for the time evolution of H can be derived using Maxwell's equation and Ohm's law (Finn & Antonsen 1985):

$$\frac{\partial H}{\partial t} = -2\int (\mathbf{E} \cdot \mathbf{B} - \mathbf{E^p} \cdot \mathbf{B^p})dV + \int (\mathbf{A} + \mathbf{A^p}) \times (\mathbf{E} - \mathbf{E^p}) \cdot \mathbf{dS} \tag{10}$$

Here $\nabla \times \mathbf{E^p} = -\partial \mathbf{B^p}/\partial \mathbf{t}$. One can further expand the non-potential terms in Eq.(9) for no-mass flux boundaries ($V_n = 0$), and write:

$$\frac{\partial H}{\partial t} = -2\eta \int \mathbf{J} \cdot \mathbf{B} dV + \eta \int \mathbf{A} \times \mathbf{J} \cdot \mathbf{dS} + \int (\mathbf{A} \cdot \mathbf{v})(\mathbf{B} \cdot \mathbf{dS}) + ... \tag{11}$$

The first and second terms represent helicity decay by Ohmic dissipation. Helicity can also be injected into the system by the tangential plasma flow on the boundaries represented by the third term in Eq.(11), e.g. via footpoint motion. For the calculation with fixed footpoints, this term vanishes, and helicity can only dissipate resistively. We use this to assess the influence of the numerical resistivity on the solution since the dissipation rate of H is proportional to the effective value of resistivity in the code (see Appendix).

To compute H from Eq.(9), the potential field $\mathbf{B}^p = \nabla \times \mathbf{A^p}$ consistent with the boundary conditions of our numerical solution must be determined. On the top and bottom boundaries we set B_n^p equal to the value B_z found from our solution, while at the side boundaries B_n^p is set equal to zero. For cases with moving footpoints, the potential field must be computed at each time step. The solution for $\mathbf{A}^p$ is calculated in Coulomb gauge $\nabla \cdot \mathbf{A}^p = 0$:

$$\nabla \times \mathbf{B}^p = \nabla \times \nabla \times \mathbf{A}^p = -\nabla^2 \mathbf{A}^p = 0.$$

This equation is solved only for A_x^p and A_y^p. We can set A_z^p to zero since $J_z^p = 0$ on the boundaries. Boundary conditions for A_x^p and A_y^p are derived from the specified B_n^p and the Coulomb gauge condition. At $z = 0$ we have:

$$\frac{\partial A_x^p}{\partial x} + \frac{\partial A_y^p}{\partial y} = 0$$

$$\frac{\partial A_y^p}{\partial x} - \frac{\partial A_x^p}{\partial y} = B_z(x, y)$$

To automatically satisfy the Coulomb gauge condition, we introduce a new variable ψ:

$$A_x^p = -\frac{\partial \psi}{\partial y};\ A_y^p = \frac{\partial \psi}{\partial x},$$

and then solve Laplace's equation

$$\frac{\partial^2 \psi}{\partial^2 x} + \frac{\partial^2 \psi}{\partial^2 y} = B_z(x, y) \tag{12}$$

with null Dirichlet boundary conditions $\psi = 0\ at\ x = 0, L_x;\ y = 0, L_y$.

At the $x = 0, L_x$ boundaries we set A_y^p to the value found at the bottom boundary

$$-\frac{\partial A_y^p}{\partial z} = B_x = 0; A_y^p(y, z) = A_y^p(y, 0);$$

and derive the Neumann boundary condition for A_x^p from the Coulomb gauge:

$$\frac{\partial A_x^p}{\partial x}(y, z) = -\ \frac{\partial A_y^p}{\partial y}(y, z)$$

Similarly at $y = 0, L_y$ we set A_x^p to the value found at the bottom boundary:

$$\frac{\partial A_x^p}{\partial z} = B_y = 0; A_x^p(x, z) = A_x^p(x, 0);$$

and find the Neumann boundary condition for A_y^p from the Coulomb gauge:

$$\frac{\partial A_y^p}{\partial y}(x,z) = -\frac{\partial A_x^p}{\partial x}(x,z)$$

Finally, we calculate A_x^p and A_y^p at the top boundary $z = L_z$ by solving Eq.(11) for ψ with Neumann boundary conditions taken from the bottom surface:

$$\frac{\partial \psi}{\partial x} = \frac{\partial \psi}{\partial x}|_{z=0} \ at \ x = 0, L_x; \ \frac{\partial \psi}{\partial y} = \frac{\partial \psi}{\partial y}|_{z=0} \ at \ y = 0, L_y$$

This finishes the specifications of the problem for solving $\nabla^2 \mathbf{A}^p = 0$ with derived boundary conditions.

3. Simulation Results

3.1. Parallel Equal Flux Tubes

First we investigate a cohelicity case - two flux tubes of equal strength with parallel axial fields B_z. To check the influence of the numerical resistivity on the solution, we performed calculations with the electrical resistivity set to zero, corresponding to the ideal MHD regime. The footpoints were allowed to move. The attracting flux tubes push against each other forming a thin line current anti-parallel to the initial current. The tubes continue to attract until the line current becomes so strong that its repulsive force balances the attractive force and an equilibrium is reached. If the grid is not fine enough, the numerical resistivity will lead to "reconnection". Our computational tests show that the medium grid (200x200x20) allows us to avoid this "numerical reconnection" in the ideal MHD computations for times in which the system reaches equilibrium. Further tests of the influence of numerical resistivity are presented in the Appendix.

Results for the resistive calculation of equal parallel flux tubes with moving footpoints are presented in Figs. 1-3 (Case 1.a). Figure 1 shows traces of magnetic field lines at different times during the calculation. The flux tubes attract each other and reconnect along the whole axial length, reaching a steady state solution with a single flux tube. As the flux tubes approach each other, the twist in the flux tubes gradually decreases. The twist in the final flux tube is lower than in the initial configuration (see from Fig. 1). Figure 2 shows the solution at the $z = L_z/2$ midplane. During the evolution to a steady state, the diameter of the final flux tube gradually increases to about twice the diameter of the initial tubes. Thus although the currents add, the twist of final flux tube is lower the that of the initial tubes. Figure 3 shows the time evolution of magnetic energy (Curve 1) and helicity (Curve 6) of the system, normalized to their initial values. Figure 3 also shows the time history of the changes in the plasma thermal (Curve 4) and kinetic (Curve 5) energies, both normalized to the initial magnetic energy E_0. At the end of the run, the plasma kinetic energy has gone to zero and the increase in thermal energy equals the loss of magnetic energy.

The volume integral of magnetic energy $\mathbf{B}^2/2\mu_0$ is governed by the following equation:

$$\frac{\partial}{\partial t}\int \frac{\mathbf{B}^2}{2\mu_0}dV = -\int (\mathbf{J}\times\mathbf{B})\cdot\mathbf{v}dV - \int \eta\mathbf{J}^2 dV - \int \frac{\mathbf{E}\times\mathbf{B}}{\mu_0}\cdot\mathbf{dS} \tag{13}$$

The volume integral of $(\mathbf{J}\times\mathbf{B})\cdot\mathbf{v}$ is the work done on the plasma by the electromagnetic force, the volume integral of $\eta\mathbf{J^2}$ is resistive dissipation which includes reconnection, and the surface integral in Eq.(13) is a Poynting's flux through the boundaries. The Poynting's flux is zero for cases with fixed footpoints.

For Case 1.a, 13% of the initial magnetic energy has been released, while the magnetic helicity declined only by 1% in the final steady state, as can be seen by comparing Curves 1 and 6 in Fig. 3. Until $t \simeq 12$, magnetic energy is released mostly through work done on plasma by the electromagnetic force (Curve 2 in Fig. 3), and goes into plasma kinetic energy (Curve 5 in Fig.3). This kinetic energy is eventually deposited as plasma thermal energy (Curve 4 in Fig. 3). In the final state about 10% of the initial magnetic energy release is through work on the plasma by the electromagnetic force, and 3% is due to resistive dissipation (Curve 3 in Fig. 3). The resistive dissipation rapidly increases at $t \simeq 12$ as the flux tubes merge via reconnection. As the system goes to an equilibrium state, the magnetic energy is released mostly by the much more gradual resistive dissipation associated with ordinary Ohmic dissipation with no reconnection. No significant magnetic energy and helicity flux through the top and bottom boundaries is observed. The lower twist of the final flux tube appears somewhat surprising since helicity is nearly conserved. However, the final and initial state of the system has the same amount of helicity since the diameter of the final flux tube with less twist is wider by about a factor of two than the initial flux tubes with larger twist (Eq. 8). Thus the final flux tube is more stable to the kink mode than the initial flux tubes. The observational studies of coronal structures provided some evidence (Pevtsov & Canfield 1996) that in cohelicity reconnection of stable flux tubes, the twist may add up to make the final flux tube unstable. In these observations, however, a longer flux tube was created from reconnection at adjacent footpoints of the two initial flux tubes so that the overall length of the flux tube increased. We simulated a case in which the axial length of the final single flux was constrained to be the same length as that of the initial flux tubes.

Results for parallel equal flux tubes with fixed footpoints (Case 1.b) are presented in Figs. 4-5. Here reconnection takes place only near the middle of the domain, as can be seen from the magnetic field line traces in Fig. 4. The final magnetic field configuration has two flux tubes turning around each other. The twist of the flux tubes decreased, while magnetic helicity declined by about 1% (Curve 6 in Fig. 4). The energy and helicity time evolution in Case 1.b are similar to Case 1.a with moving footpoints (compare Figs. 3 and 5). Even though the reconnection takes place only in a small region for the Case 1.b, nearly the same amount of magnetic energy has been released as in Case 1.a. The maximum kinetic energy is less for Case 1.b than for Case 1.a, an expected difference between moving and fixed footpoints.

3.2. Antiparallel equal flux tubes

Next we investigate the interaction of two equal strength flux tubes and antiparallel axial fields B_z. In this case both poloidal and axial magnetic field components can reconnect. Because the flux tubes have the same amount of twist but of opposite sign, the total magnetic helicity is zero. Figures 6-8 show results for calculations with moving footpoints (Case 2.a). The flux tubes attract and annihilate the axial magnetic field (Fig. 6). The overshoot of axial magnetic field observed at t=32 in Fig. 6 is consistent with experimental results (Yamada et al. 1997). During the simulation the helicity H stays equal to zero (Fig. 7, Curve 6), which is consistent with a final state with no B_z due to the reconnection (Fig. 6). Note that in the final state 20% of the initial magnetic energy is left (Curve 1, Fig. 7), whereas almost 100% of the initial magnetic energy went into the thermal energy of plasma (Curve 4, Fig. 7). This apparent discrepancy is explained by a non-zero net Poynting's flux through the top and bottom boundaries, which supplies additional magnetic energy to the computational domain. We believe that the increase in magnetic energy (Curve 1, Fig. 7) at t=25 is due to this external magnetic energy, since it is absent for the Case 2.b with fixed footpoints (Curve 1, Fig. 10). Note that more of the initial magnetic energy is dissipated by work on the plasma by the electromagnetic force than in the Case 1.a. For the Case 2.a, the system reaches a steady state more slowly and the kinetic energy (Curve 5, Fig. 7) is more prominent than for the Case 1.a. Strong flows with velocities greater than the sound speed but less than V_A can be observed in Fig. 8. These flows, which develop in both the X-Y plane and in the Z direction, subside as the solution reaches a steady state. The final magnetic configuration (Fig. 6, t=270) has no B_z, i.e. the pressure of the poloidal magnetic field is balanced by the high beta plasma pressure within the tube - consistent with experimental observations (Fig. 6) (Yamada et al. 1997). Thus the low-beta initial configuration has been transformed into a high-beta configuration. The observed sausage perturbations of the plasma pressure in Fig. 8 are consistent with the perturbations allowed by a plasma with only a poloidal magnetic field.

The results for antiparallel equal flux tubes with fixed footpoints (Case 2.b) are presented in Figs. 9-10. The flux tubes reconnect in the middle and, as the system evolves, the loops unwind (Fig. 9). The final state consists of two arcs attached to the top and bottom boundaries. These two arcs are untwisted as expected since the total magnetic helicity of the system is zero. In this case, no magnetic energy is supplied through the boundaries. In the final state, 70% of initial magnetic energy has been deposited as thermal energy and 30% is stored in the final magnetic configuration (Curves 1,4 in Fig. 10). Unlike the case with fixed footpoints (Case 1.b), the plasma flows here play an important role in the system evolution (Curve 5, Fig. 10.).

We have also compared the rates of poloidal magnetic field reconnection for counterhelicity (Case 2.a) and cohelicity (Case 1.a) simulations with moving footpoints. To describe the reconnection quantitatively, we study the time evolution of A_z contours in X-Y midplane (Fig. 11). Here A_z is a flux ψ function for the poloidal component of the magnetic field. Let us define ψ_c as the value of the common flux in the center of the X-Y plane, and ψ_p as the peak flux of each tube. The ratio of $a_c = \psi_c/\psi_p$ is plotted in Fig. 12. Complete reconnection corresponds to $a_c = 1$. The reconnection proceeds faster for counterhelicity than for cohelicity, consistent with experiments (Yamada et al. 1997). The time derivative of ψ_c is the reconnection rate of poloidal magnetic field. The reconnection rate was calculated in the linear growth phase (Fig. 12) between t=5 and t=20 for both cohelicity and counterhelicity cases. For the cohelicity case the reconnection rate is 0.06, while for the counterhelicity case the rate is 0.11. We can compare these values with the

Sweet-Parker and Petschek models of steady reconnection for a one-dimensional current sheets. The reconnection rate $\dot{\psi}_{SP}$ for the Sweet-Parker model is

$$\frac{\partial\psi}{\partial t} = \dot{\psi}_{SP} = v_A B_e S_0^{-1/2}$$

where B_e is the magnitude of the reconnected magnetic field, and S_0 is the corresponding Lundquist number (Sweet 1958; Parker 1963). The Sweet-Parker model assumes reconnection proceeds in a region with a length about the macroscopic size of the system, and is usually referred as slow reconnection. In contrast, the Petschek model assumes that reconnection is localized in a region much smaller than the macroscopic spatial scale, and is known as a fast-reconnection model (Petschek 1964). Both models assume steady-state reconnection. The reconnection rate $\dot{\psi}_P$ for the Petschek model is given by

$$\frac{\partial\psi}{\partial t} = \dot{\psi}_P \simeq v_A B_e (\ln S_0)^{-1}$$

Substituting our parameters $v_A = 1$, $B_e = 1$ and $S_0 = 10^3$ into the above expressions, we obtain $\dot{\psi}_{SP} \simeq 0.033$ and $\dot{\psi}_P \simeq 0.147$. Thus our computed reconnection rates fall between those predicted by the Sweet-Parker and Petschek models. Note however, that ours is not a steady-state reconnection rate.

For the case with parallel flux tubes, the time scale for both reconnection and relaxation to a steady state are about the same - a few tens of τ_A. In contrast, the evolution to steady state is considerably slower for the case of antiparallel flux tubes because of the strong supersonic (but subalfvenic) flows developing during reconnection.

3.3. Nonequal Antiparallel flux tubes

Here we investigate the reconnection of two flux tubes with opposite axial magnetic fields and a 10% difference in B_0 in the Gold-Hoyle flux tubes (see Sec. 2.2).

Results for a case with moving footpoints case are presented in Figs. 13-14 (Case 3.a). The steady state magnetic configuration has a substantial nonuniform distribution of magnetic field on X-Y midplane (Fig. 13). One can observe significant qualitative differences between this simulation and Case 2.a with equal antiparallel flux tubes. At t=24, Fig. 13 shows an overshoot in axial magnetic field similar to Case 2.a. However, the magnetic flux tubes then separates into three tubes, one having B_z and J_z in the opposite direction from the others (see t=100, Fig. 13). This configuration of fields and currents seems to increase the rate of the resistive dissipation of helicity, i.e. the $\eta \int \mathbf{J} \cdot \mathbf{B} dV$ term in Eq. (11). The two flux tubes with positive "orientation" seem to reconnect poloidal field with each other (see t=100 and t=226, Fig. 13). In the steady state (t=226 in Fig. 13), there is a region in the center of the domain with a very strong B_y component, which is absent at the same time for Case 3.a (Fig. 6). This is a remarkable qualitative difference given only a 10% change in the magnitude of one flux tube. There is a significant Poynting's flux through the top and bottom surfaces, apparently increasing the magnetic energy by 30% of its initial value E_0, since in steady state the thermal energy (Curve 4, Fig. 14) increased by 110% of E_0, while 20% of the initial magnetic energy (Curve 2) is stored in the final magnetic configuration. Between t=150 and t=250 the magnetic helicity drops sharply by 40% (Curve 6, Fig. 14). This is comparable with the percentage drop of the magnetic energy in the same time period. Note, that the helicity is normalized to its initial value; the absolute value of the helicity is small compared to Cases 1.a and 1.b.

In the fixed footpoints non-equal antiparallel simulations (Case 3.b), the final magnetic field configuration is similar to the case with equal antiparallel flux tubes: two arc-like structures as shown in Fig. 9. The magnetic energy (Curve 6) and helicity (Curve 4) evolution are shown in Fig. 15. An interesting feature of this simulation is that the dissipation rates of helicity and energy are comparable. In the final steady state, 40% of helicity and 60% of magnetic energy have dissipated.

4. Conclusions

We have presented results from the first 3-D resistive MHD computations which follow the interaction of Gold-Hoyle flux tubes to a final steady state. We followed the time evolution of energy and helicity of the system and obtained qualitative agreement with experimental results (Yamada et al. 1997) on 3-D magnetic reconnection. The reconnection proceeds faster in counterhelicity than in cohelicity merging. The poloidal magnetic field reconnection rates are between those predicted by the Sweet-Parker and Petschek models. Cases with fixed footpoints had lower magnetic energy release and reached a steady state faster than cases with moving footpoints. The final flux tube in cohelicity reconnection is more stable to the kink mode than the initial flux tube. For antiparallel flux tubes with moving footpoints, we observed a significant energy flux through the boundaries. For all computed cases, magnetic energy is released primarily through work done on the plasma by the electromagnetic forces rather than through resistive dissipation. These forces create plasma flows which are finally deposited in the plasma as thermal energy. We found that plasma pressure is important for the relaxation of the system to final equilibrium even for low-beta initial conditions, and it is necessary to include these effects in the simulations. We found a large qualitative difference between the solutions for equal antiparallel flux tubes and tube differing in strength by only 10%, in agreement with experiment (Yamada, 1998). For the first time we have calculated numerically a gauge invariant relative magnetic helicity of the system and compared its evolution for all computed cases. We observed that the resistive dissipation rate of helicity may vary significantly for different computational cases, and be comparable with energy dissipation.

Acknowledgments

We thank M. Velli for his comments and useful discussions. This work was supported in part by NASA/Solar Physics and in part by the NSF Center for Research in Parallel Computation under Cooperative Agreement CCR-88809615. A portion of this work was carried out at the Jet Propulsion Laboratory, California Institute of Technology, under a contract with NASA. The JPL/Caltech CRAY used in this investigation was supported by NASA.

Appendix

The MAP3 code has been tested on the MHD problem of the stability of solar coronal loops. An isolated Gold-Hoyle flux tube can be stable or unstable to the kink mode depending on the twist of the field and the plasma beta. From a series of runs with various twists, we computed the twist threshold ($\Phi \approx 2.5\pi$) and a normalized growth rate $\gamma\tau_A$ for kink unstable Gold-Hoyle flux tubes (see Fig.16) and obtained satisfactory agreement with earlier calculations (Mikic et al. 1990). To investigate the influence of the numerical resistivity, we compared the time evolution of the magnetic helicity for three different grids and for two different values of S (Fig. 17). The top two Curves 3 and 4 are for the medium and fine grid computation with $S = 10^3$. The bottom two Curves 1 and 2 are for $S = 3 \cdot 10^2$. The numerical resistivity decreases as the grid is refined. As one can see, changing S has far greater influence on the solution than changing from one grid to another. We conclude that we can study physical phenomena with $S = 10^3$ on a medium or fine grid.

REFERENCES

Berger, M. & Field, J. 1984, J. Fluid Mech., 147, 133.

Canfield et al. 1996, ApJ, 462, 547

Dahlburg, R. B. & Antiochos, S.K. 1995, Journal of Geophys. Res., 100, 16991

Finn, J. & Antonsen, T. 1985, Comments Plasma Phys. Controlled Fusion, 9, 111

Fushiki, T.& Sakai, Jun-Ichi 1995, Solar Phys. 156, 262

Gold T., Hoyle F., MNRAS., 120, 89

Lau, Y. T. & Finn, J. M. 1996, Phys. Plasmas, 3, 3983

Mikic, Z., & Schnack, D. & van Hoven, G. 1990, ApJ., 361(2), 690

Kondrashov, D., & Keefer, D. 1997, IEEE Trans. on Magn., 33(1), 254

Ono, Y., Yamada, M., Akao, T., Tajima, T., Matsumoto, R. 1996, Phys. Rev. Letters, **76**, 3328

Ozaki, M., & Sato, T. 1997, ApJ, 481, 524

Parker E. N., 1963, ApJ., 8, 177

Petschek H. E., 1964, in AAS-NASA Symp. Physics of Solar Flares, ed. W. N. Hess (Washington, DC:NASA), 425

Pevtsov, A. & R.C. Canfield, 1996, ApJ., 473(2), 533

Rust D.M. & Kumar A., 1994, Solar Phys. 155, 69

Shimizu T., Tsuneta S., et al. 1994, ApJ, 422, 906

Sweet P. A., 1958, in Electromagnetic Phenomena in Cosmic Physics, ed. B. Lenhert (New York: cambridge Univ. Press), 123

Tsuneta S., 1996, ApJ, 456, L63

Yamada M., Ji Hsu, Carter, Kulsrud, Bretz, Jobes and Ono 1997, Physics of Plasmas, 4, 1936

Yamada M., (private communication at the "Workshop on the physics of magnetic reconnection and dynamos, Princeton Plasma Physics Laboratory, January 1998)

This manuscript was prepared with the AAS LaTeX macros v4.0.

Figure Captions

Figure 1: Time evolution of magnetic field line traces for equal parallel flux tubes with moving footpoints (Case 1.a) - cohelicity. In this case only poloidal magnetic flux reconnects.

Figure 2: Plots of magnetic vector $(B_x,\ B_y)$ field and contours of B_z in X-Y midplane for equal parallel flux tubes with moving footpoints (Case 1.a).

Figure 3: Time evolution for equal parallel flux tubes with moving footpoints (Case 1.a): 1- magnetic energy E/E_0, 2-magnetic energy release through work by electromagnetic force, 3-magnetic energy release through to Ohmic dissipation, 4-change in thermal energy E_{th}/E_0, 5-change in kinetic energy E_k/E_0, 6- helicity H/H_0. Note that at early times, much of the magnetic energy goes into plasma kinetic energy. The kinetic energy tends to zero as steady state is reached. By the end of the run, all the released magnetic energy has been deposited in the plasma as thermal energy.

Figure 4: Time evolution of magnetic field line traces for equal parallel flux tubes with fixed footpoints (Case 1.b).

Figure 5: Time evolution for equal parallel flux tubes with fixed footpoints (Case 1.b): 1-magnetic energy E/E_0, 2-magnetic energy release due to work by electromagnetic force, 3-magnetic energy release due to Ohmic dissipation , 4-change in thermal energy E_{th}/E_0, 5-change in kinetic energy E_k/E_0, 6- helicity H/H_0.

Figure 6: Plots of magnetic vector field and contours of B_z in X-Y midplane for equal antiparallel flux tubes with moving footpoints - counterhelicity, Case 2.a.

Figure 7: Time evolution for equal antiparallel flux tubes with moving footpoints (Case 2.a): 1-magnetic energy E/E_0, 2-magnetic energy release due to work by electromagnetic force, 3-magnetic energy release due to Ohmic dissipation , 4-change in thermal energy E_{th}/E_0, 5-change in kinetic energy E_k/E_0, 6- helicity H/H_0.

Figure 8: Plots of flow vector field and pressure contours in X-Z midplane for equal antiparallel flux tubes with moving footpoints (Case 2.a).

Figure 9: Time evolution of magnetic field line traces for equal antiparallel flux tubes with fixed footpoints (Case 2.b).

Figure 10: Time evolution for equal antiparallel flux tubes with fixed footpoints (Case 2.b): 1-magnetic energy E/E_0, 2-magnetic energy release due to work by electromagnetic force, 3-magnetic energy release due to Ohmic dissipation , 4-change in thermal energy E_{th}/E_0, 5-change in kinetic energy E_k/E_0, 6- helicity H/H_0.

Figure 11: A_z contours in the x-y midplane for equal antiparallel flux tubes with moving footpoints.

Figure 12: Comparison of reconnection rates for cohelicity and counterhelicity cases.

Figure 13: Plots of magnetic vector field and contours of B_z in X-Y midplane for nonequal antiparallel flux tubes with moving footpoints (Case 3.a).

Figure 14: Time evolution for nonequal antiparallel flux tubes with moving footpoints (Case 3.a): 1-magnetic energy E/E_0, 2-magnetic energy release due to work by electromagnetic

force, 3-magnetic energy release due to Ohmic dissipation , 4-change in thermal energy E_{th}/E_0, 5-change in kinetic energy E_k/E_0, 6- helicity H/H_0.

Figure 15: Time evolution for nonequal antiparallel flux tubes with fixed footpoints (Case 3.b):1-magnetic energy E/E_0, 2-magnetic energy release due to the work by electromagnetic force, 3-magnetic energy release due to Ohmic dissipation , 4-change in thermal energy E_{th}/E_0, 5-change in kinetic energy E_k/E_0, 6- helicity H/H_0. Note that in this case the absolute value of H_0 is much less than in Cases 1a, 1b.

Figure 16. Growth rate vs. twist for unstable Gold-Hoyle flux tube: 1- MAP3 result, 2-Mikic et al. 1990.

Figure. 17 : Time evolution of helicity for different grids and different values of input physical resistivity: 1- coarse grid and $S = 3 \cdot 10^2$, 2- medium grid and $S = 3 \cdot 10^2$, 3-medium grid and $S = 10^3$, 4- fine grid and $S = 10^3$.

t=0

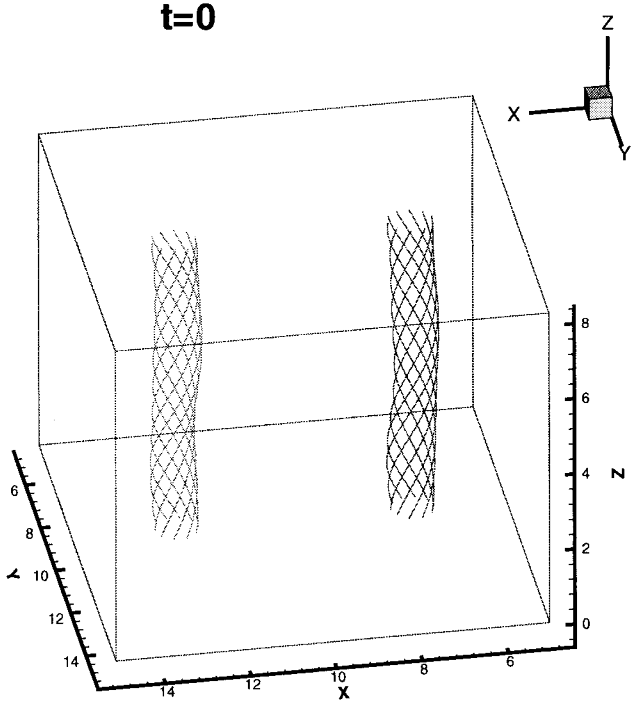
Z
X
Y
0
2
4
6
8
z
6
8
10
12
14
y
14
12
10
8
6
x

t=10

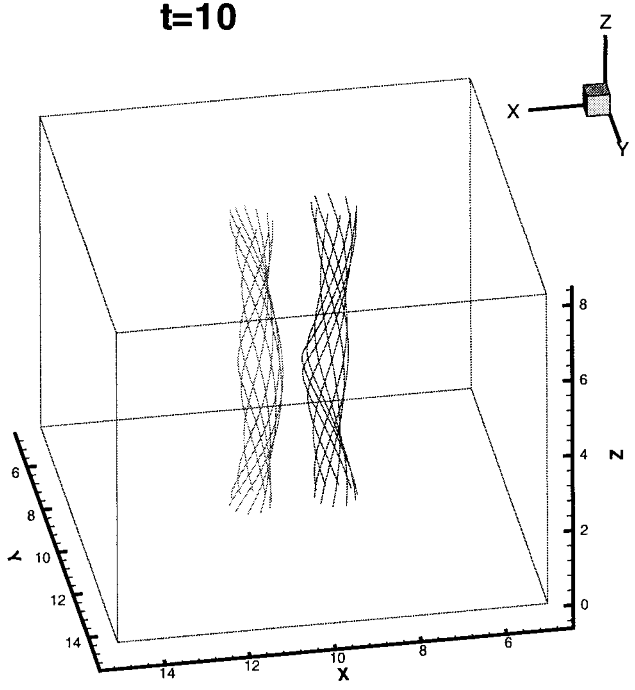
Z
X
Y
0
2
4
6
8
z
6
8
10
12
14
y
14
12
10
8
6
x

t=25

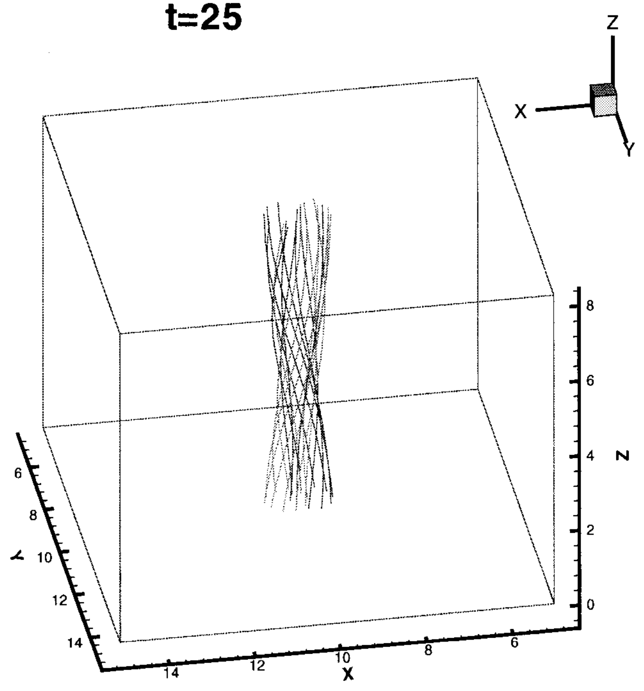
Z
X
Y
0
2
4
6
8
z
6
8
10
12
14
y
14
12
10
8
6
x

t=35

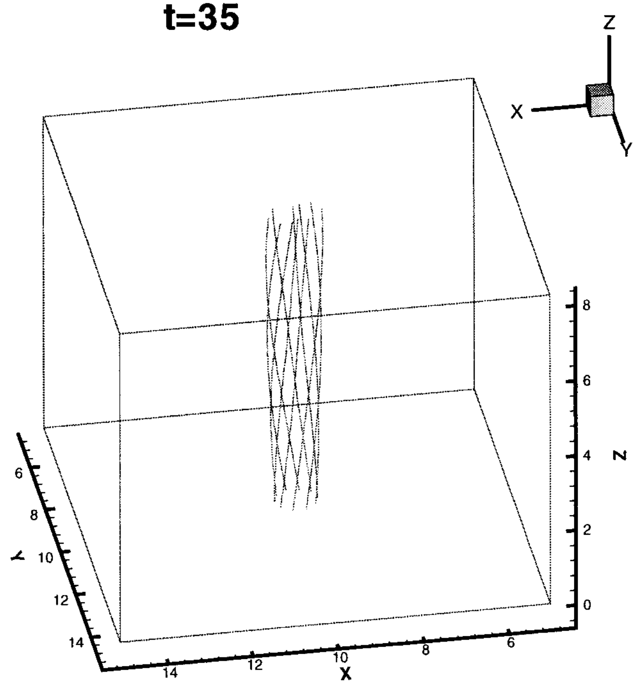
Z
X
Y
0
2
4
6
8
z
6
8
10
12
14
y
14
12
10
8
6
x

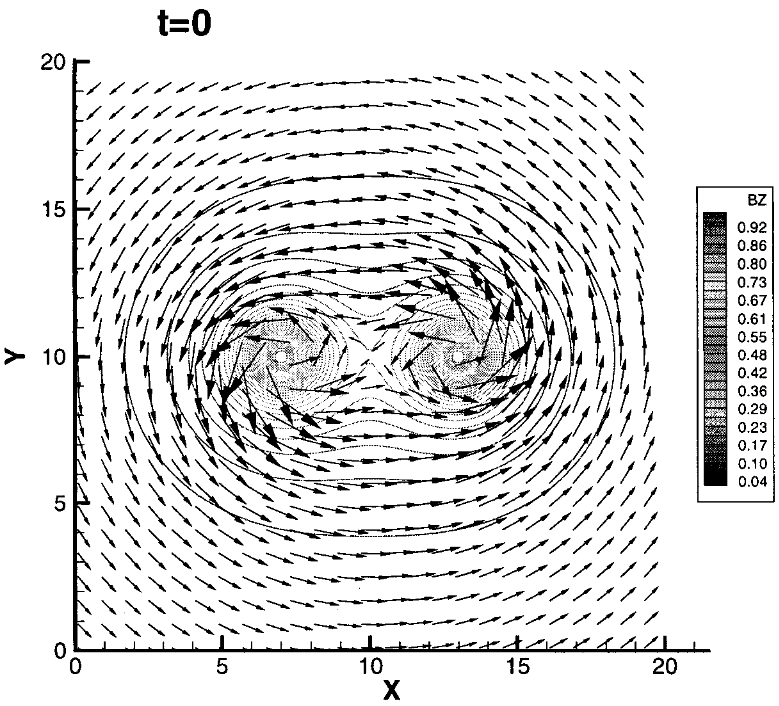
t=0
BZ
0.92
0.86
0.80
0.73
0.67
0.61
0.55
0.48
0.42
0.36
0.29
0.23
0.17
0.10
0.04
Y
0
5
10
15
20
X
0
5
10
15
20

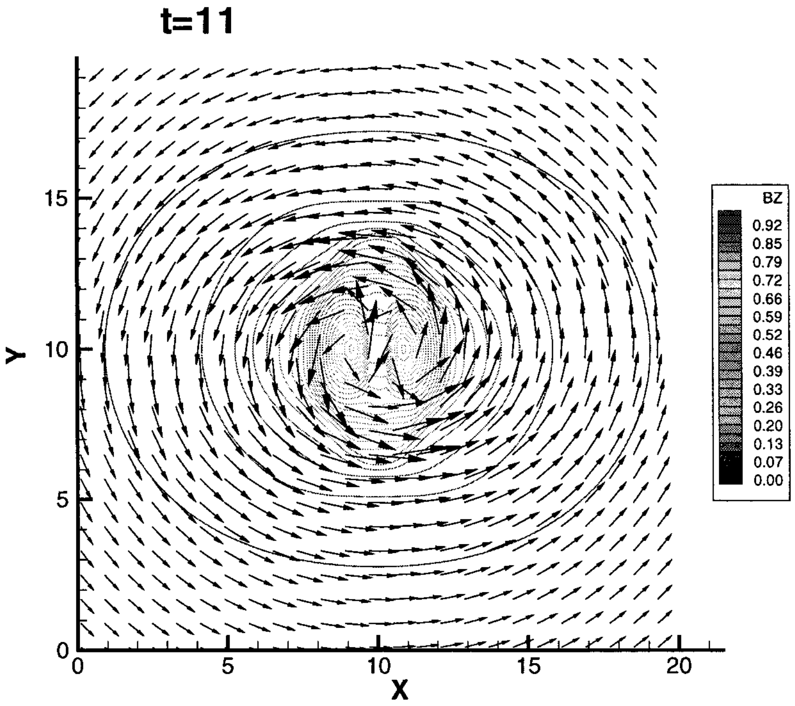
t=11
BZ
0.92
0.85
0.79
0.72
0.66
0.59
0.52
0.46
0.39
0.33
0.26
0.20
0.13
0.07
0.00
Y
0
5
10
15
X
0
5
10
15
20

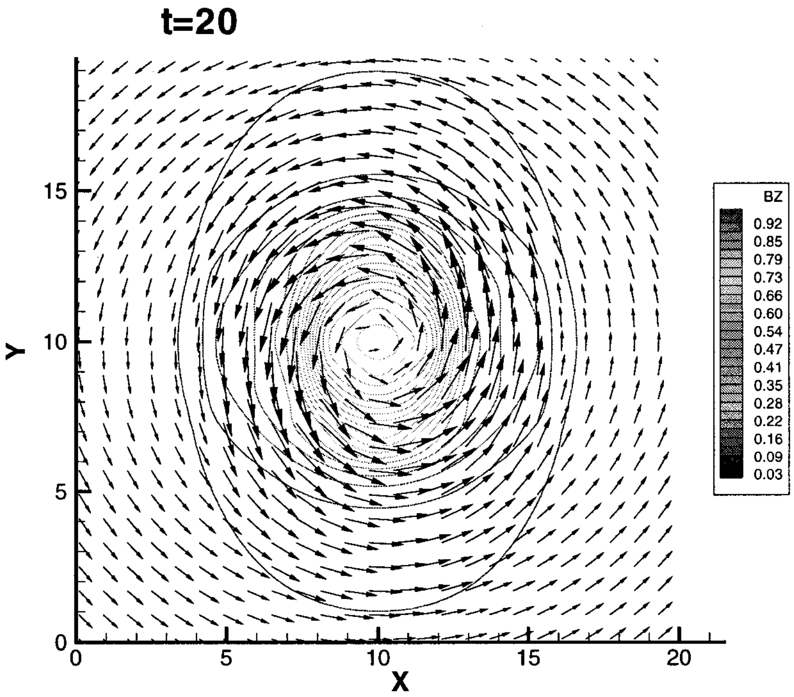
t=20
BZ
0.92
0.85
0.79
0.73
0.66
0.60
0.54
0.47
0.41
0.35
0.28
0.22
0.16
0.09
0.03
Y
0
5
10
15
X
0
5
10
15
20

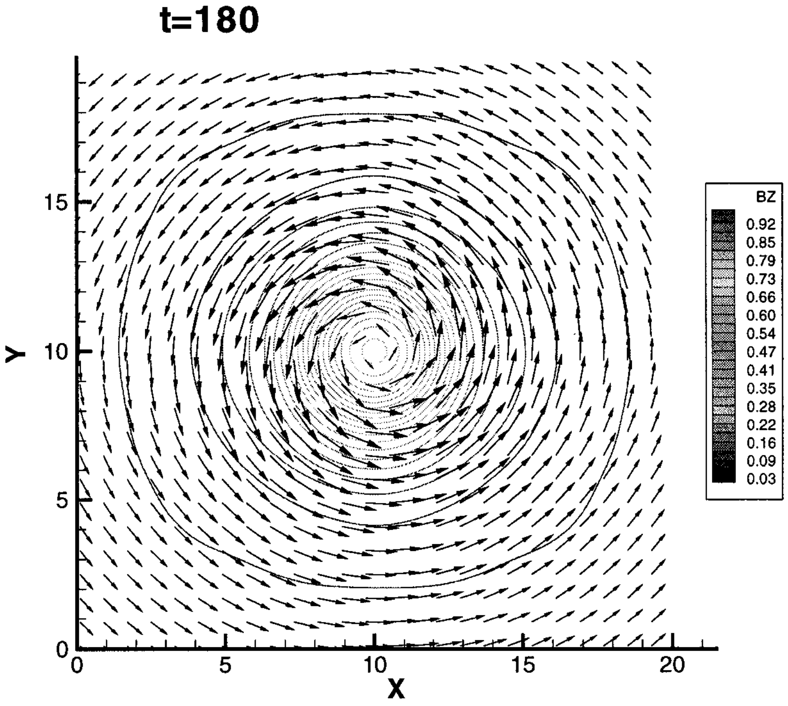
t=180
BZ
0.92
0.85
0.79
0.73
0.66
0.60
0.54
0.47
0.41
0.35
0.28
0.22
0.16
0.09
0.03
Y
0
5
10
15
X
0
5
10
15
20

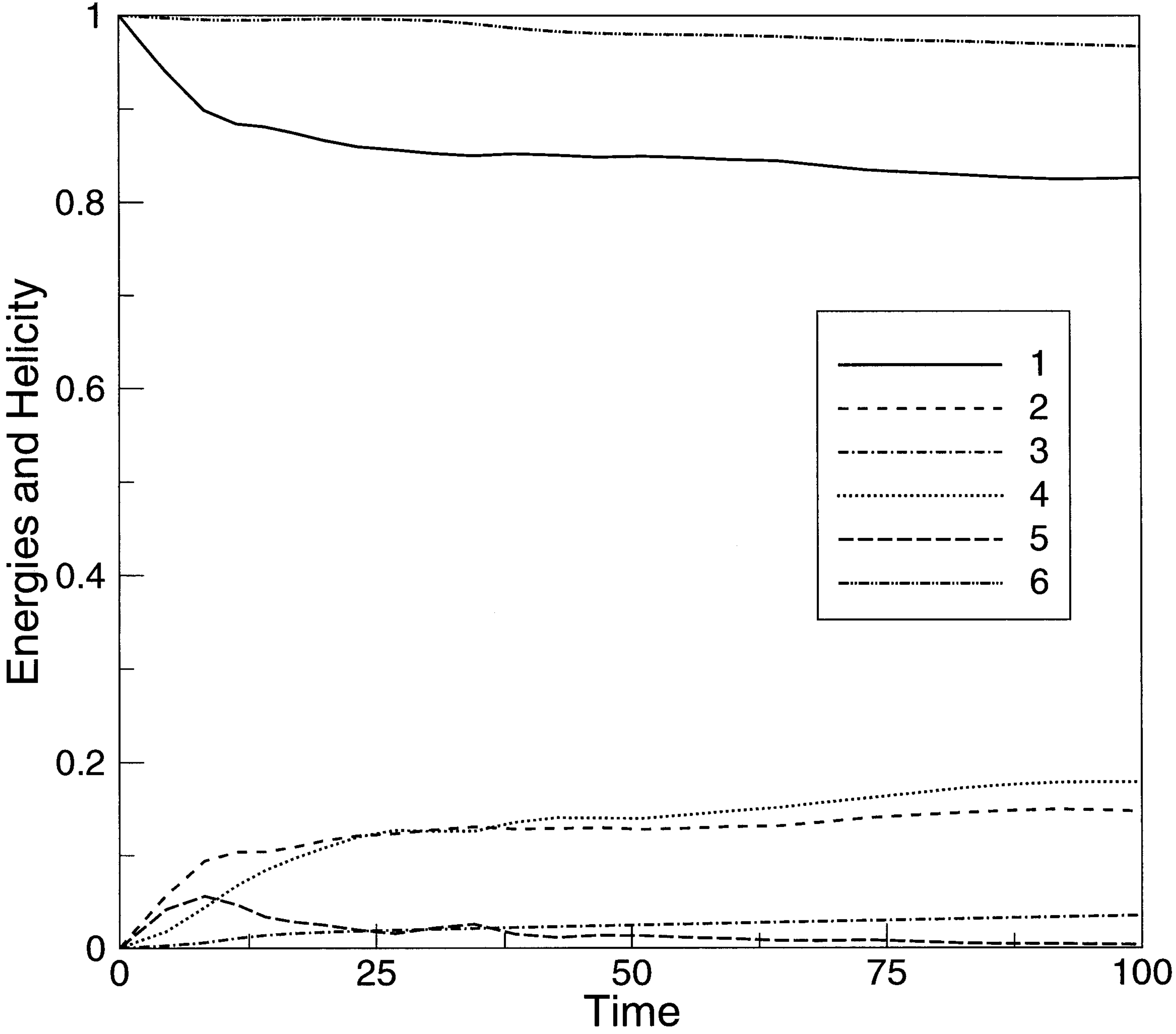

1
0.8
0.6
0.4
0.2
0
0
25
50
75
100
Time
Energies and Helicity
1
2
3
4
5
6

t=0

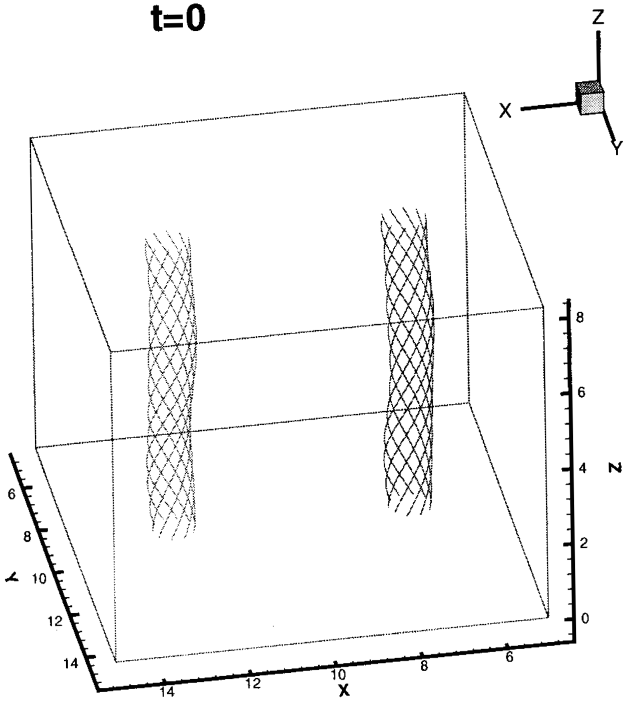
Z
X
Y
8
6
4
2
0
z
6
8
10
12
14
y
14
12
10
8
6
x

t=10

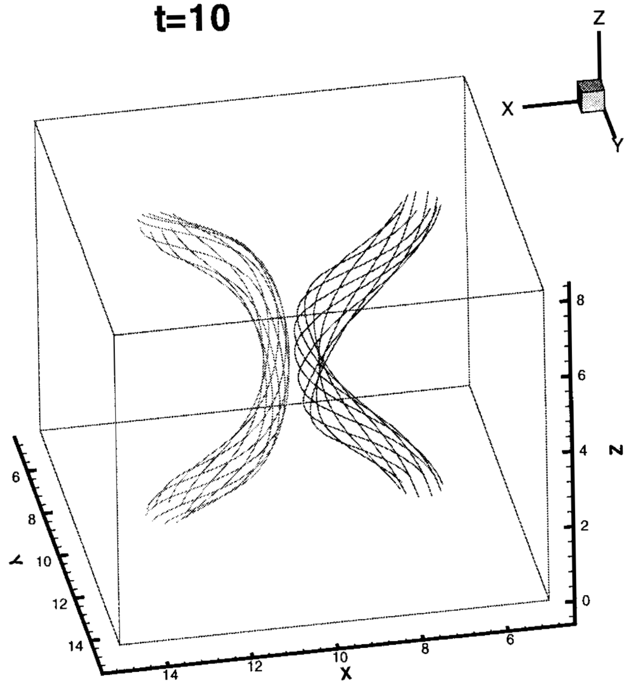
Z
X
Y
8
6
4
2
0
z
6
8
10
12
14
y
14
12
10
8
6
x

t=17

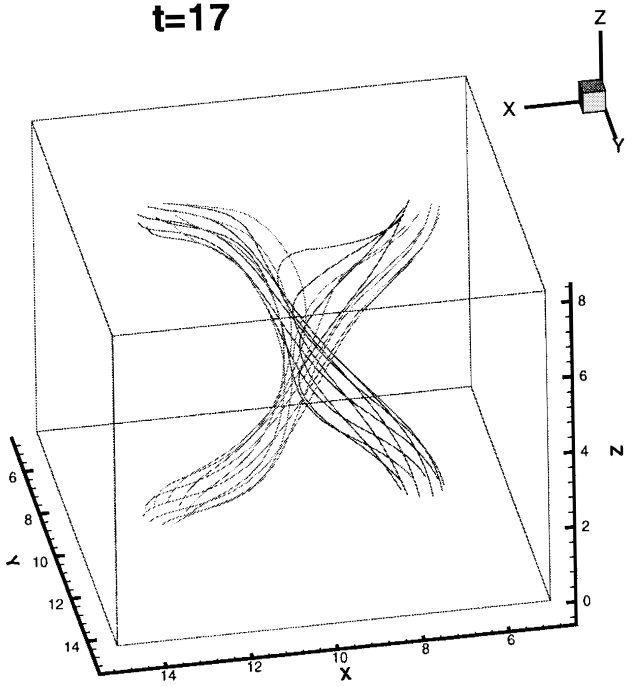
Z
X
Y
8
6
4
2
0
z
6
8
10
12
14
y
14
12
10
8
6
x

t=35

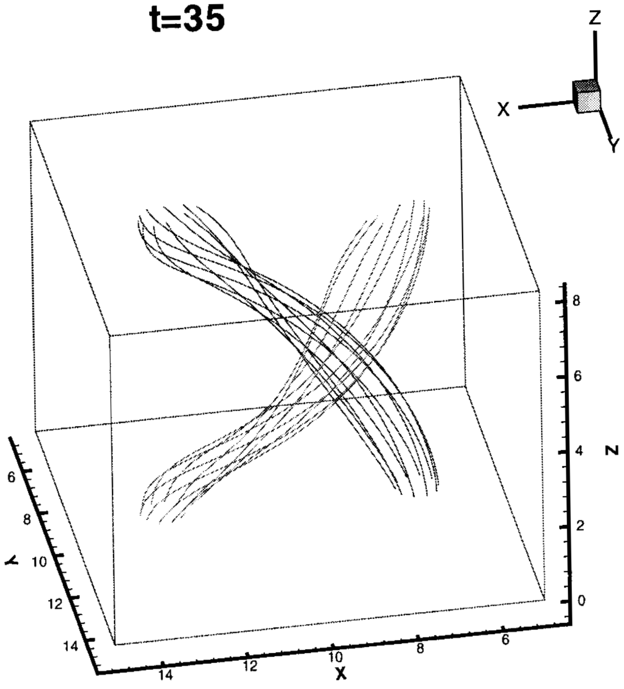
Z
X
Y
8
6
4
2
0
z
6
8
10
12
14
y
14
12
10
8
6
x

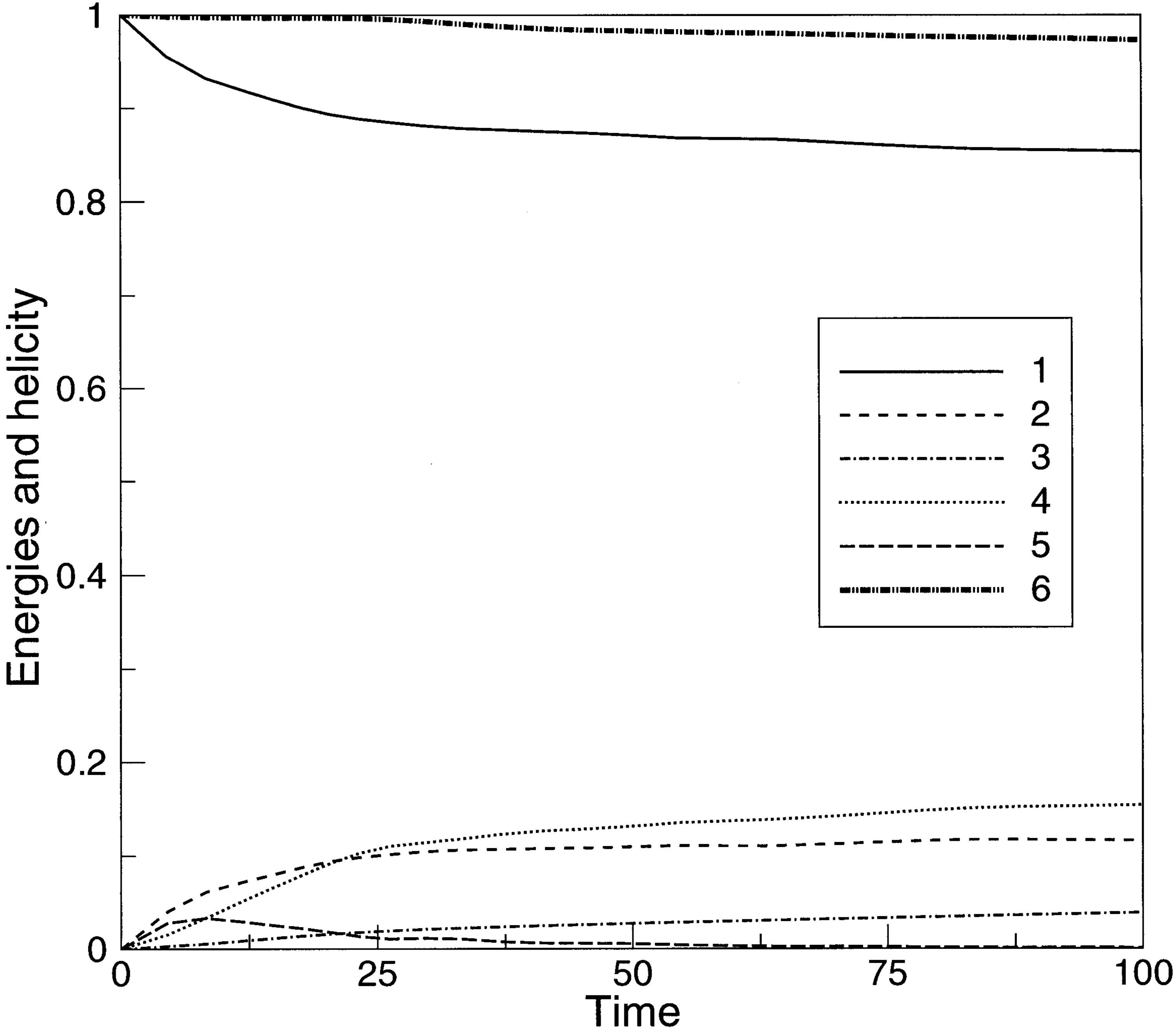
Energies and helicity
Time
0
0.2
0.4
0.6
0.8
1
0
25
50
75
100
1
2
3
4
5
6

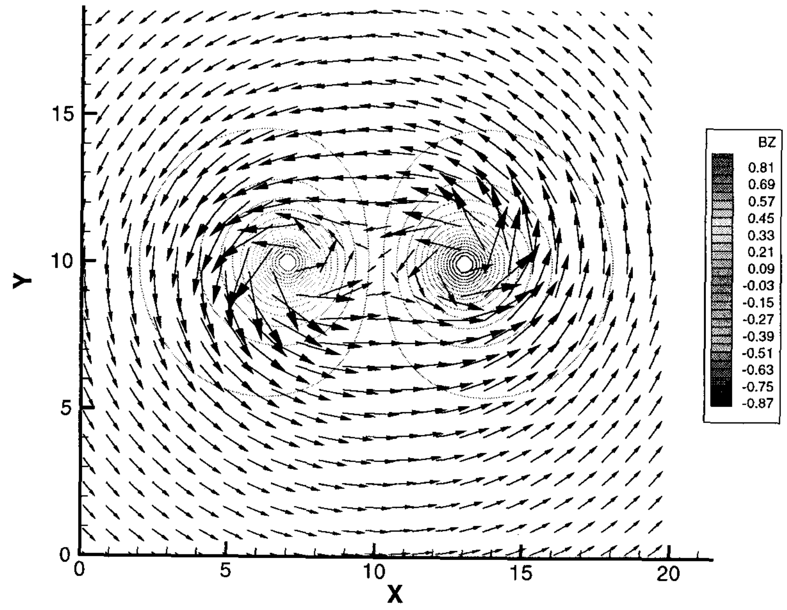
t=0

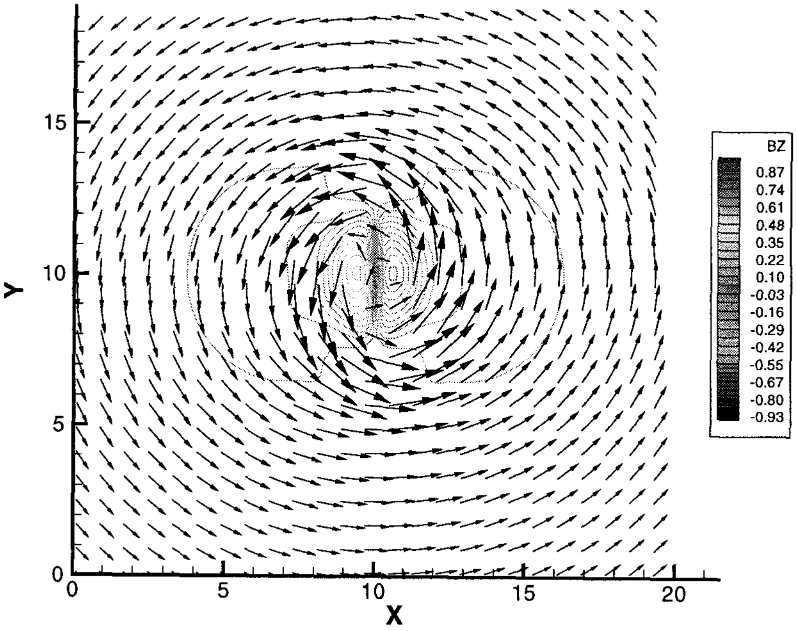
t=11

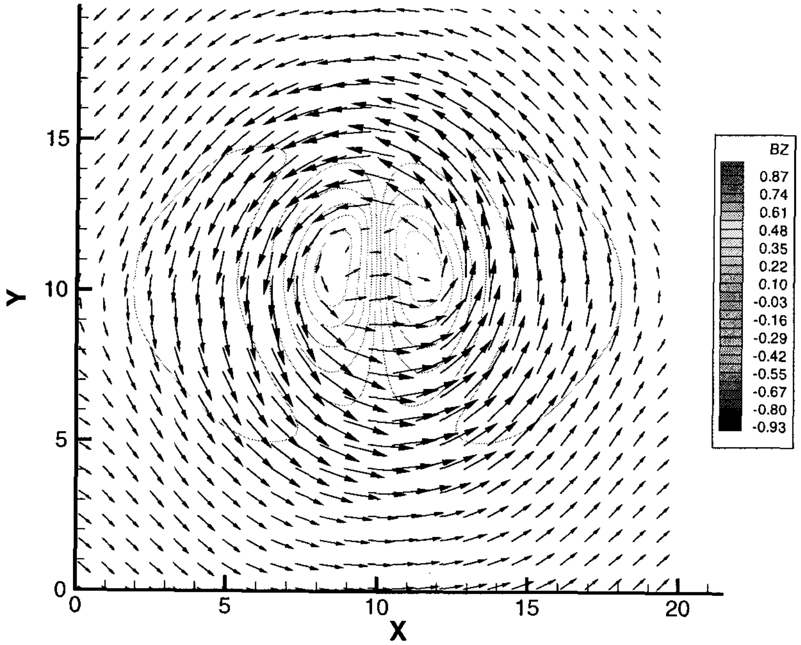
t=32

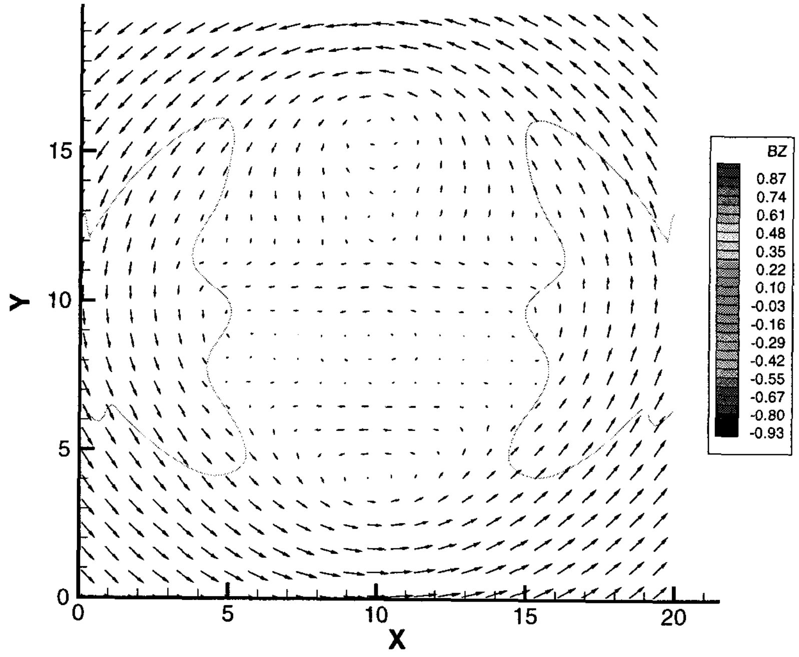
t=270

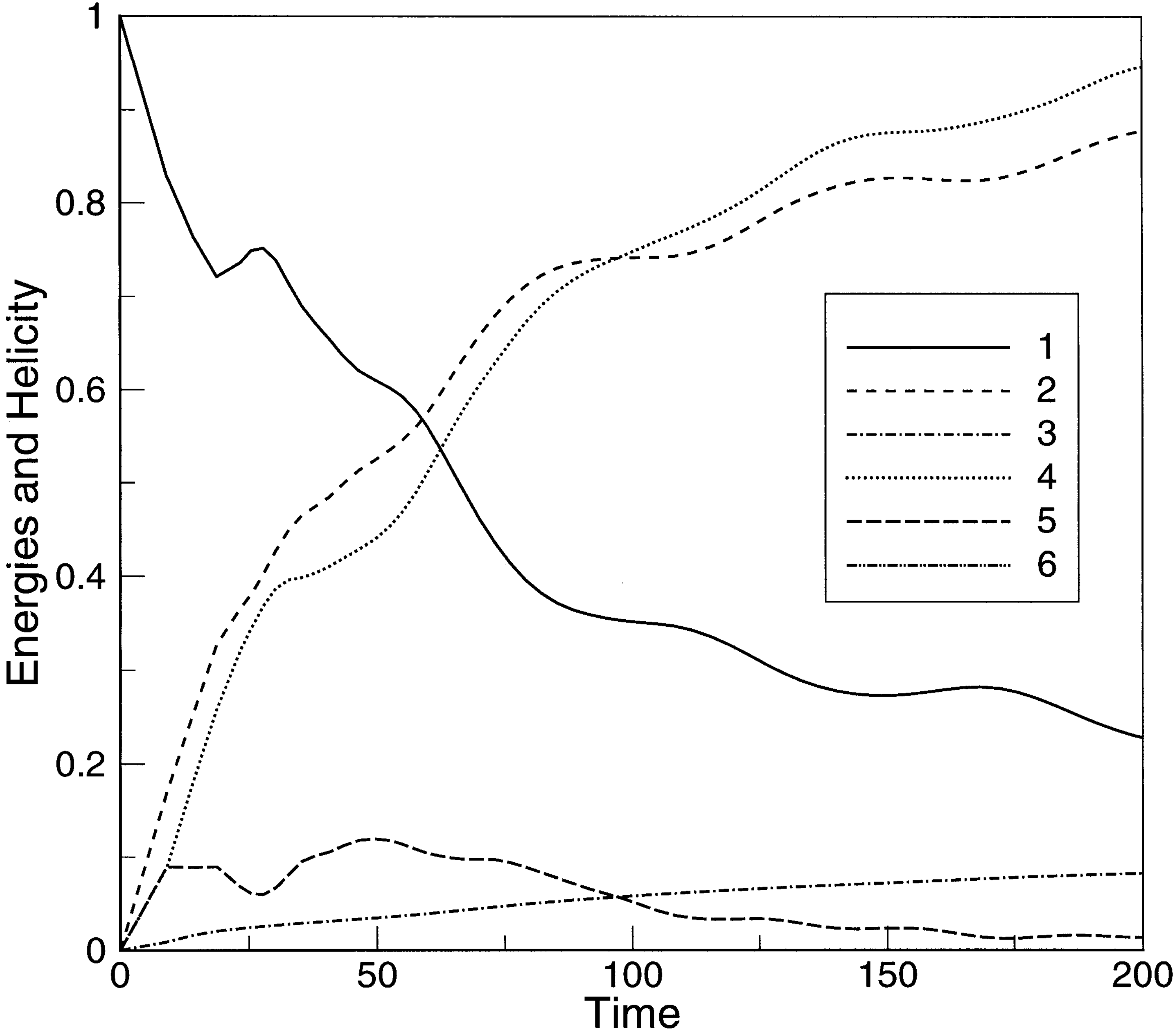
Energies and Helicity
Time
0
0.2
0.4
0.6
0.8
1
0
50
100
150
200
1
2
3
4
5
6

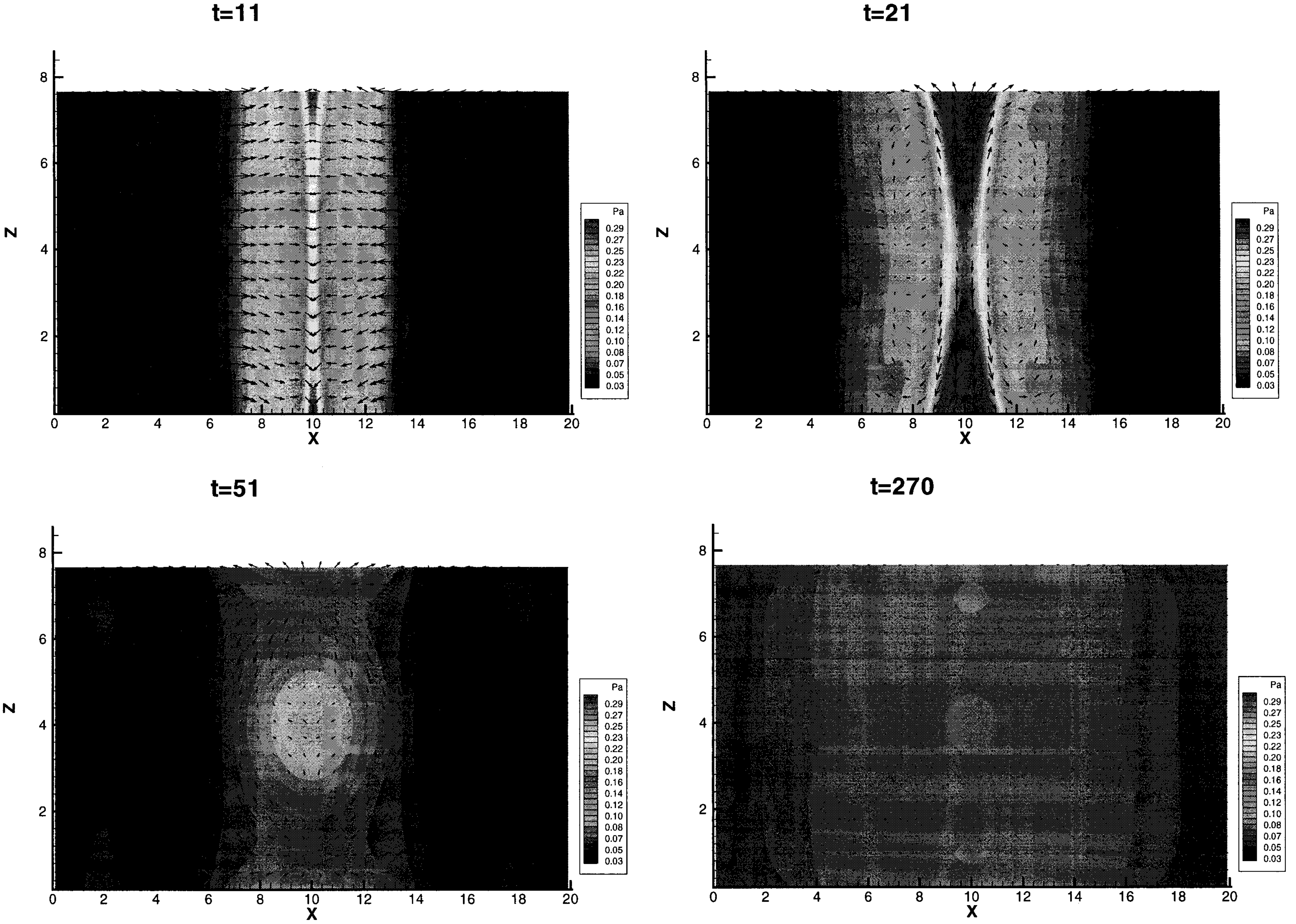
t=11
t=21
t=51
t=270
Z
X
0
2
4
6
8
10
12
14
16
18
20
Pa
0.29
0.27
0.25
0.23
0.22
0.20
0.18
0.16
0.14
0.12
0.10
0.08
0.07
0.05
0.03

t=0

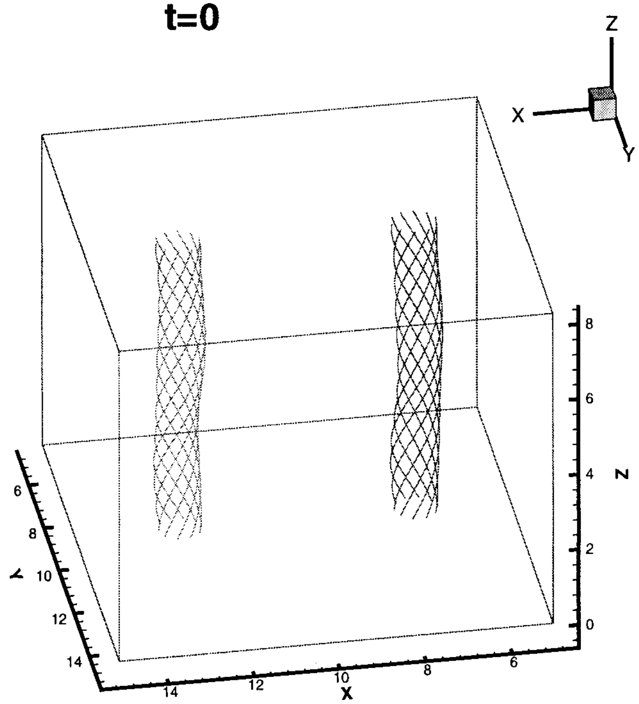

t=10

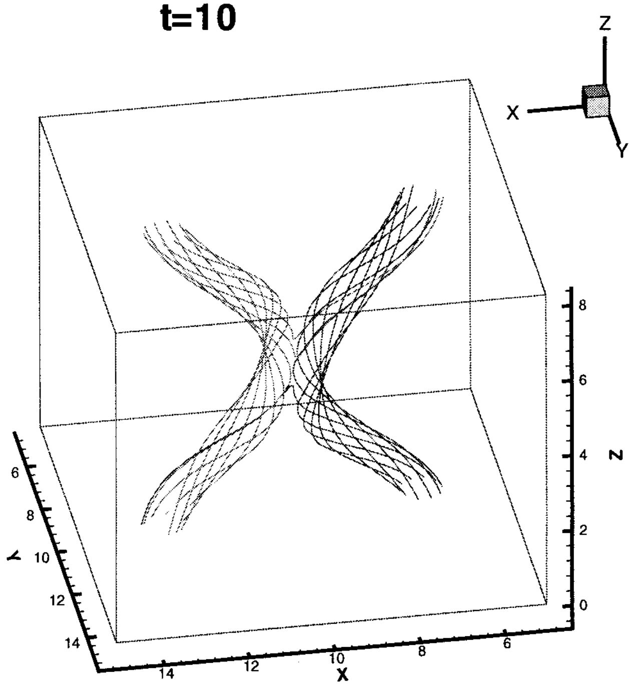

t=15

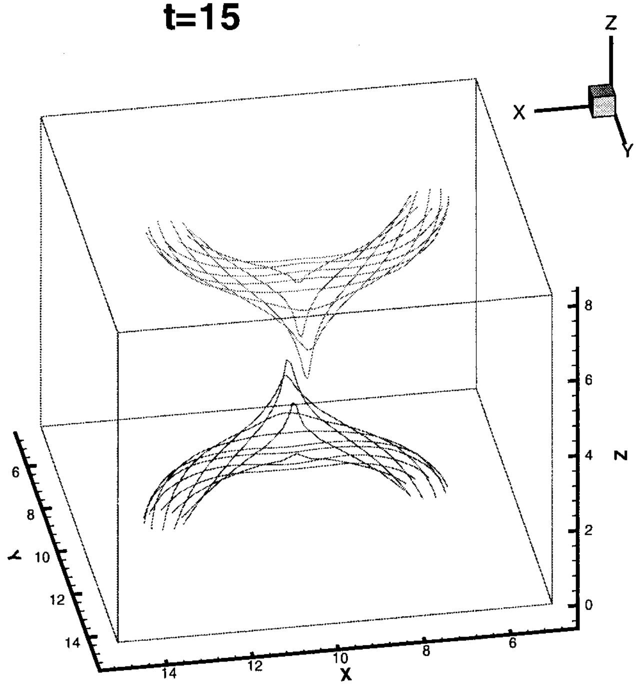

t=25

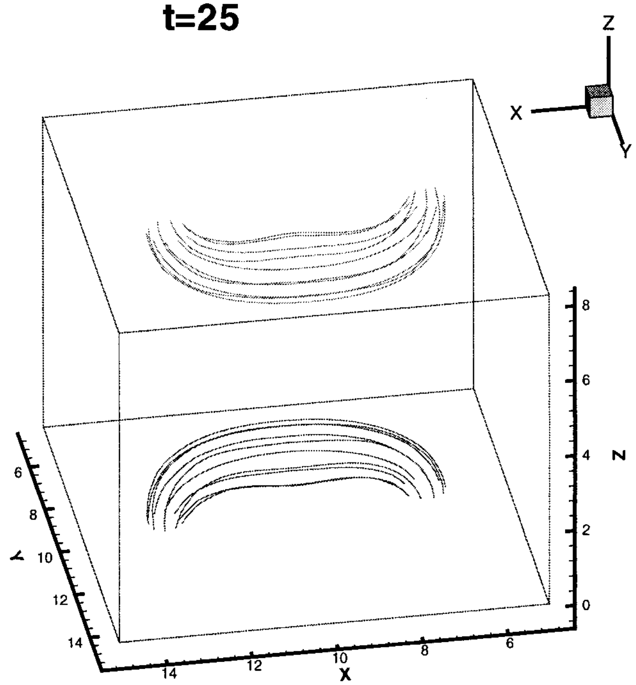

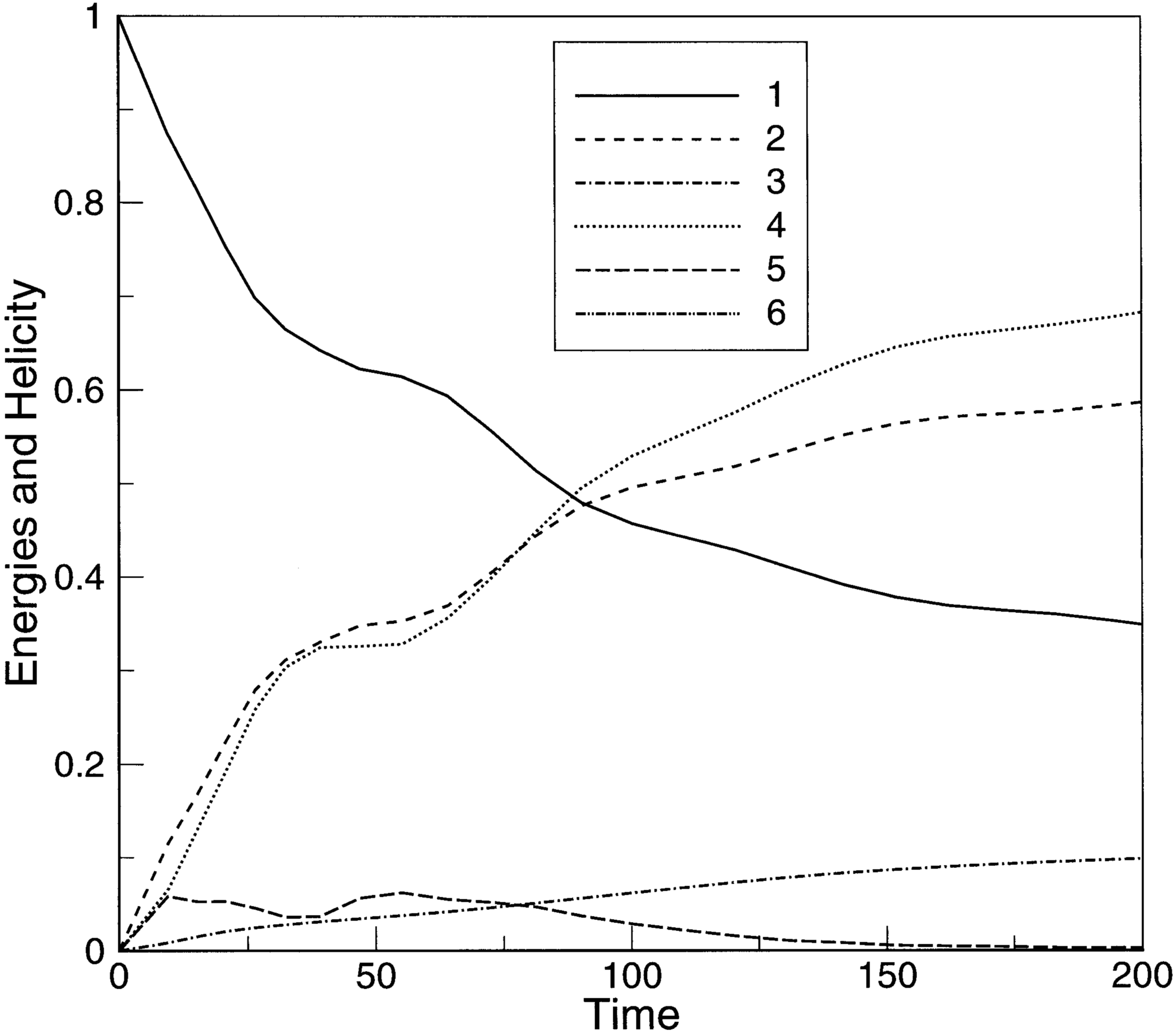

1
0.8
0.6
0.4
0.2
0
Energies and Helicity
0
50
100
150
200
Time
1
2
3
4
5
6

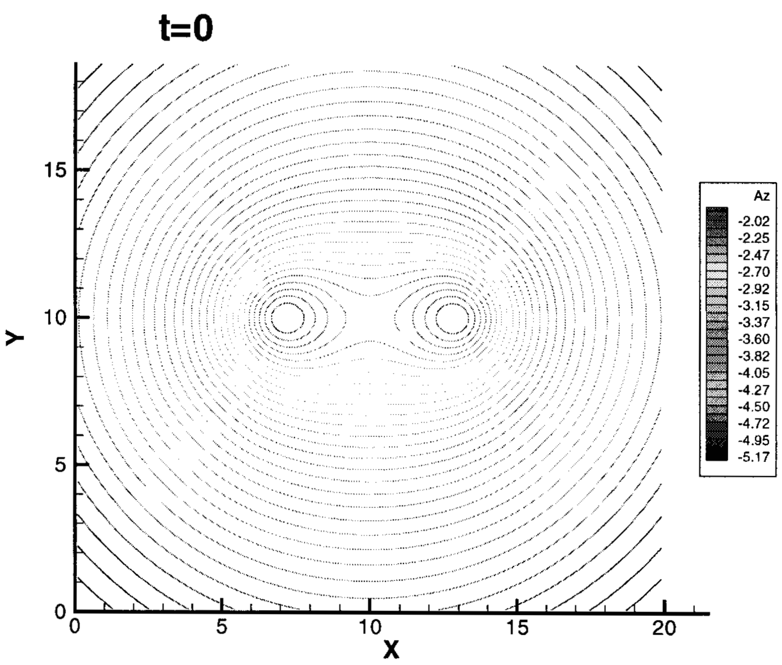
t=0

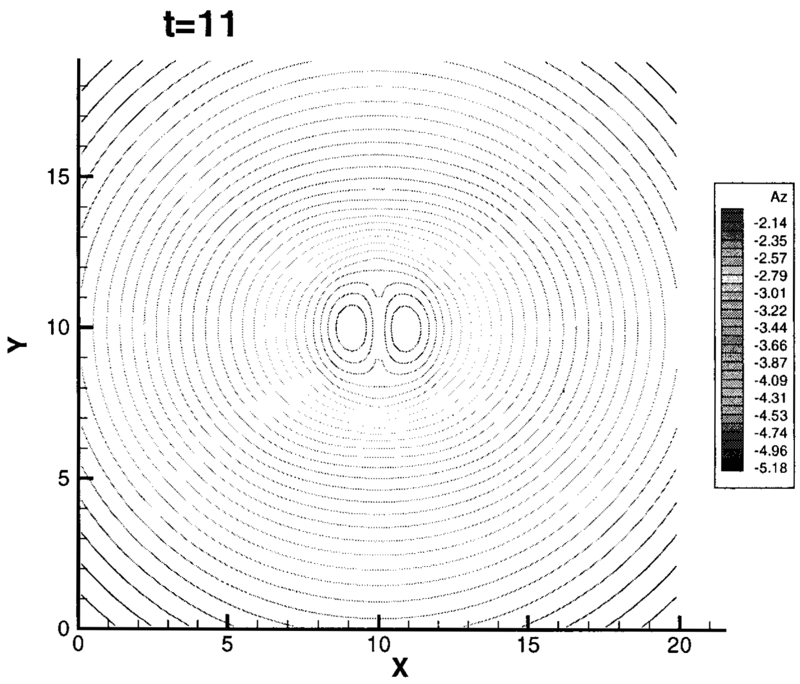
t=11

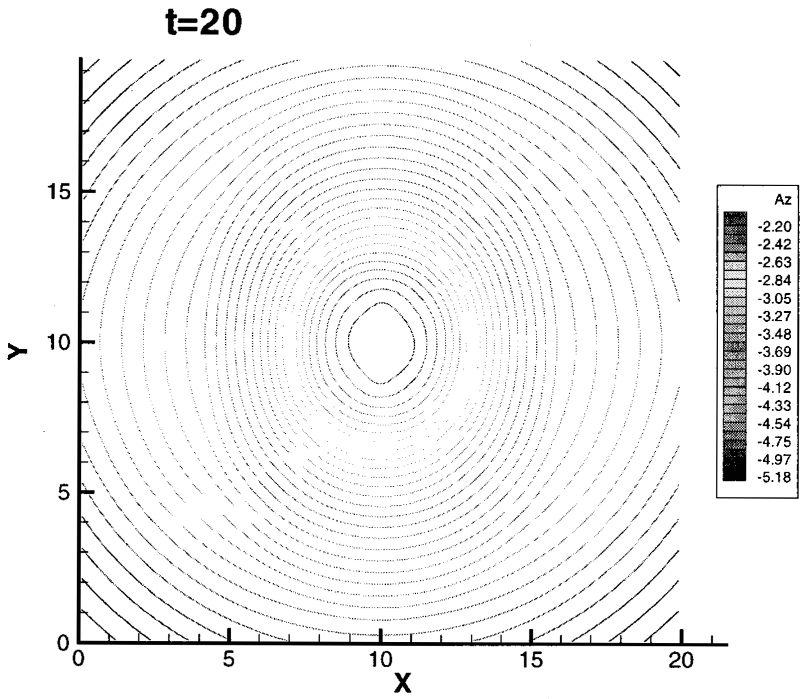
t=20

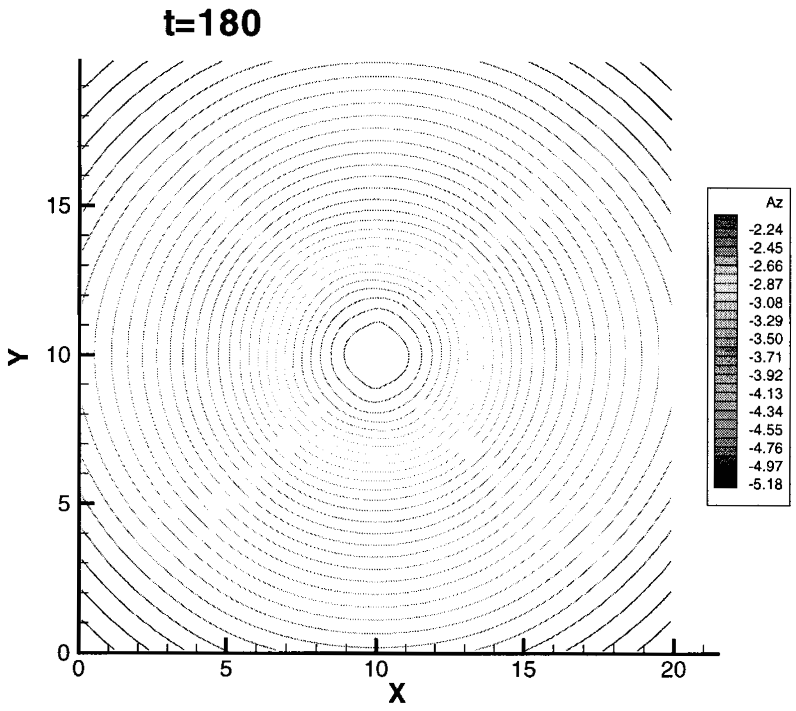
t=180

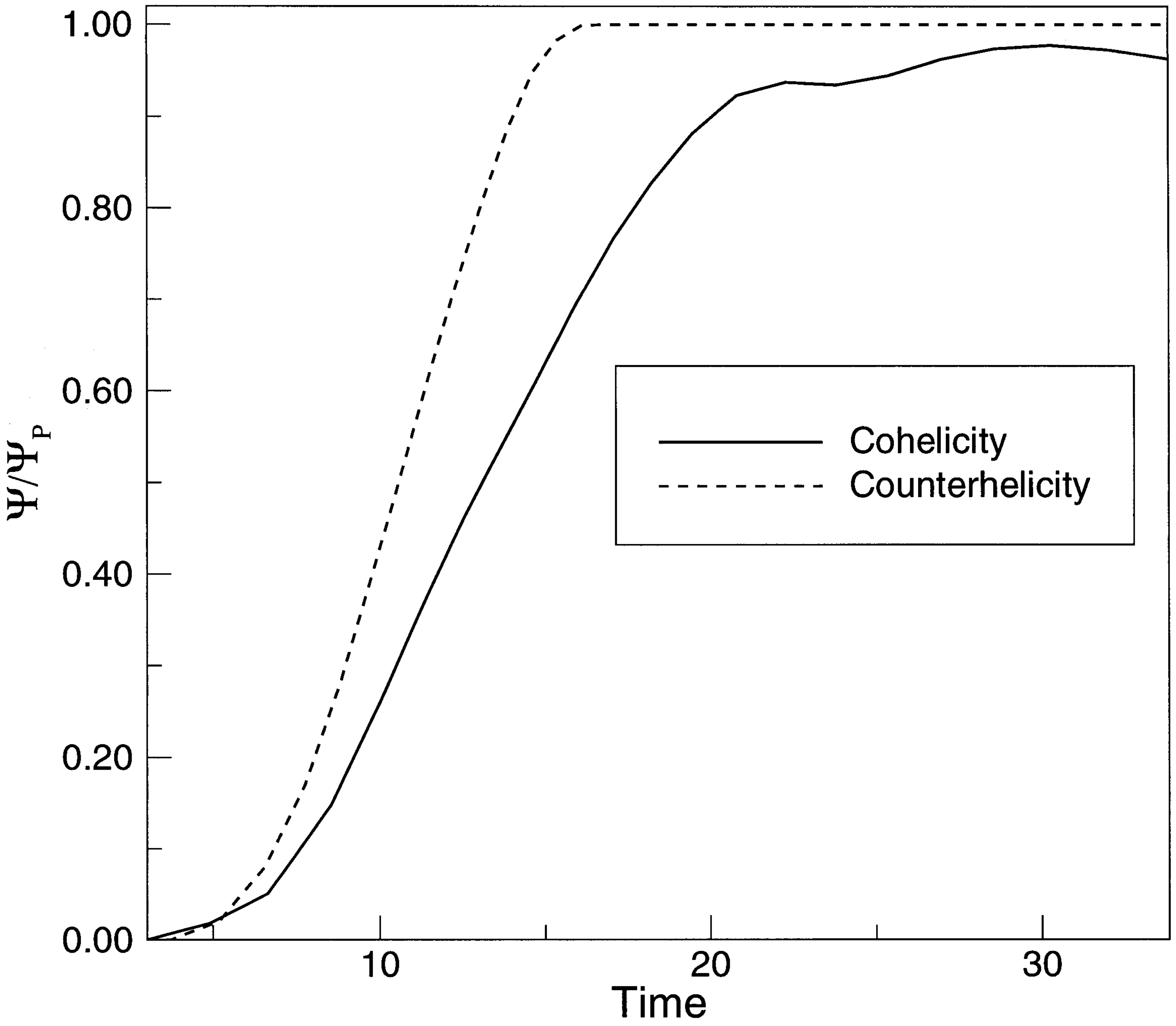
1.00
0.80
0.60
0.40
0.20
0.00
Ψ/Ψ_P
10
20
30
Time
Cohelicity
Counterhelicity

t=0

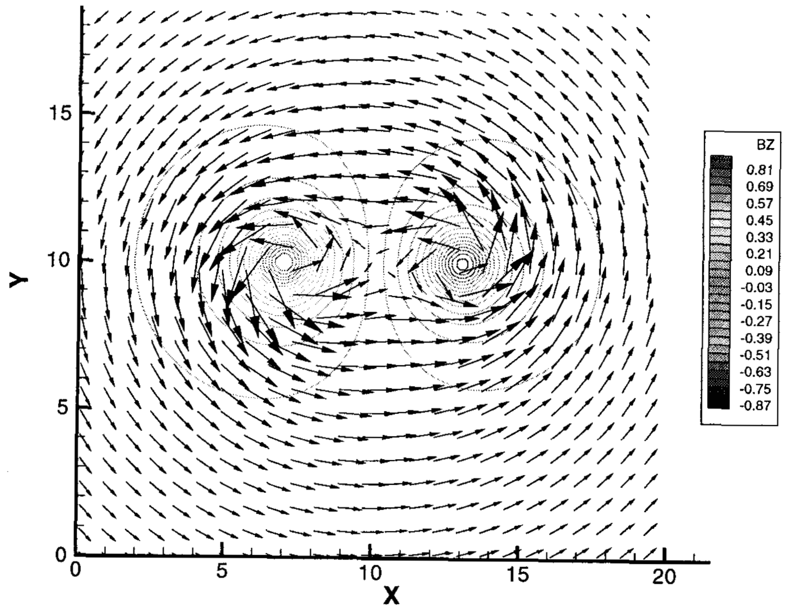

t=24

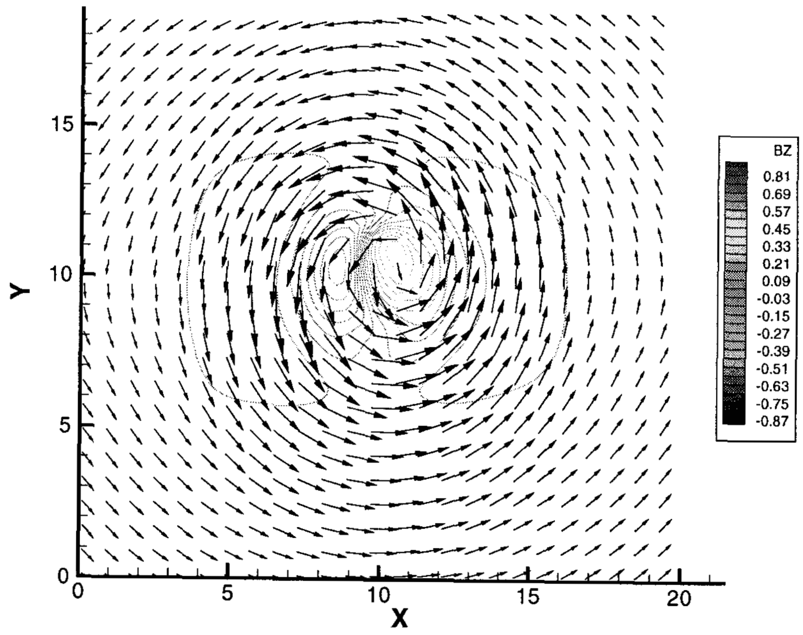

t=100

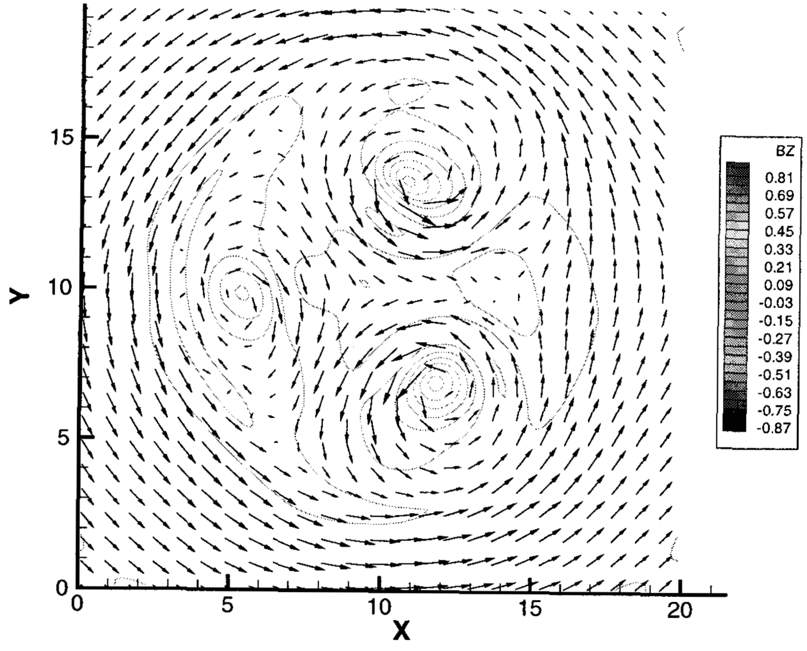

t=226

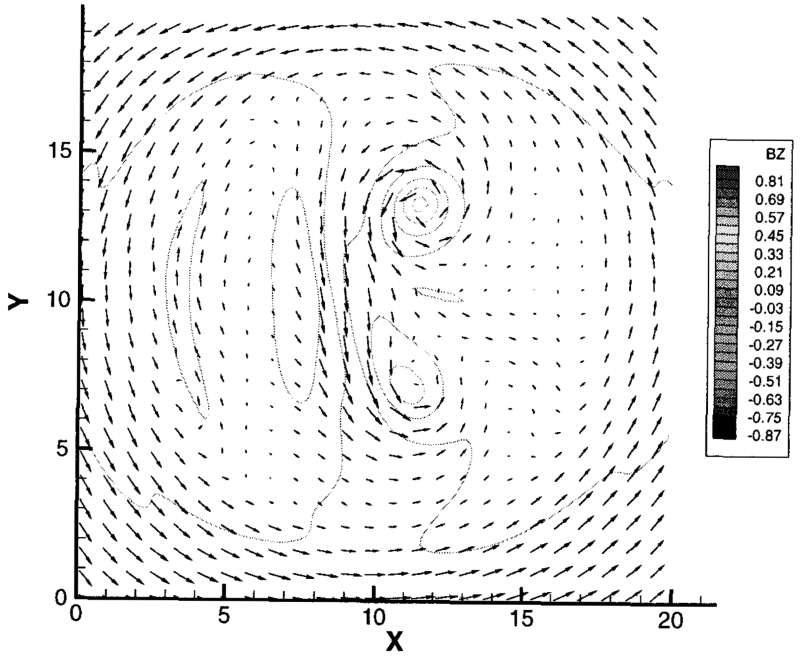

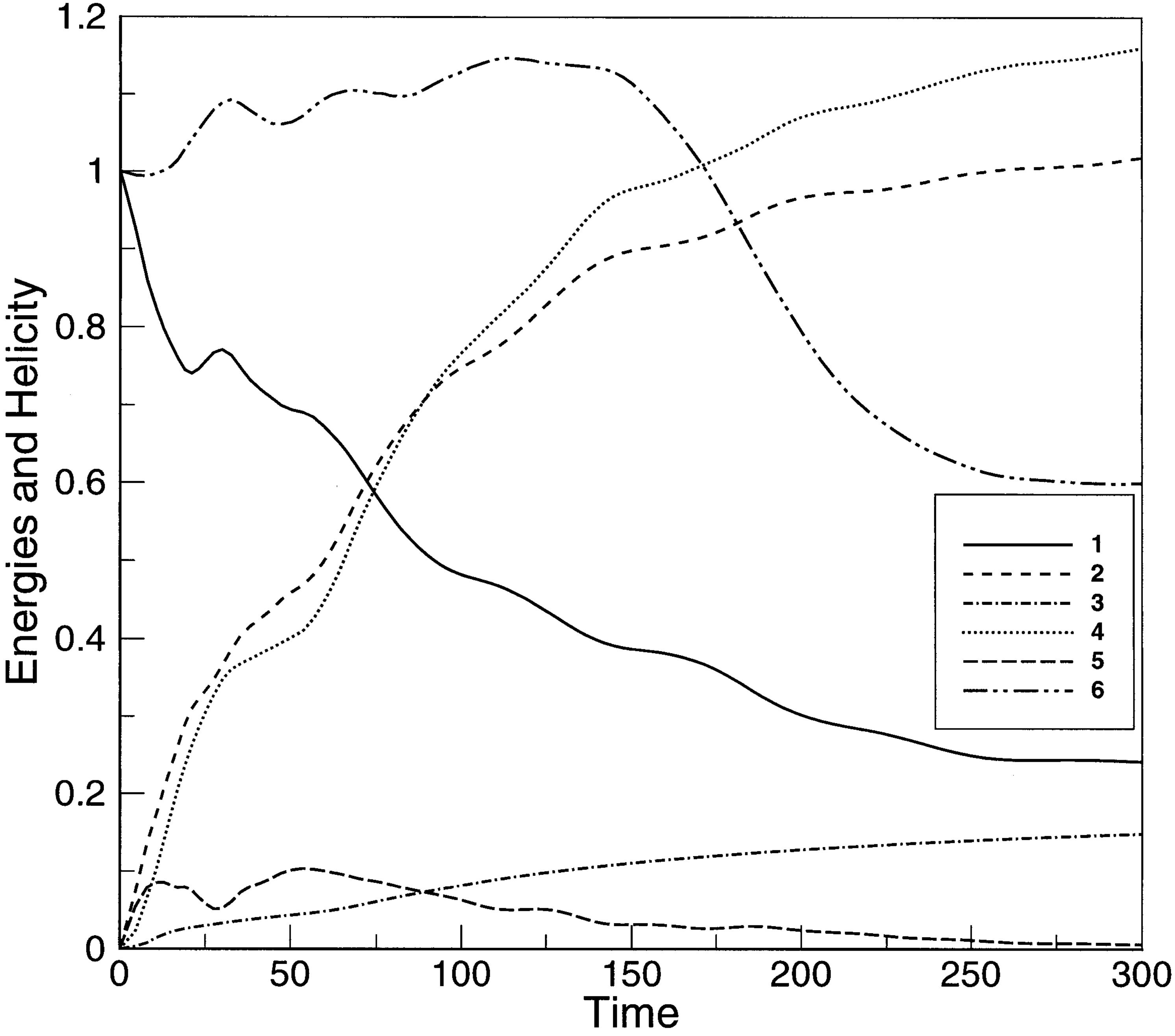

1.2
1
0.8
0.6
0.4
0.2
0
Energies and Helicity
0
50
100
150
200
250
300
Time
1
2
3
4
5
6

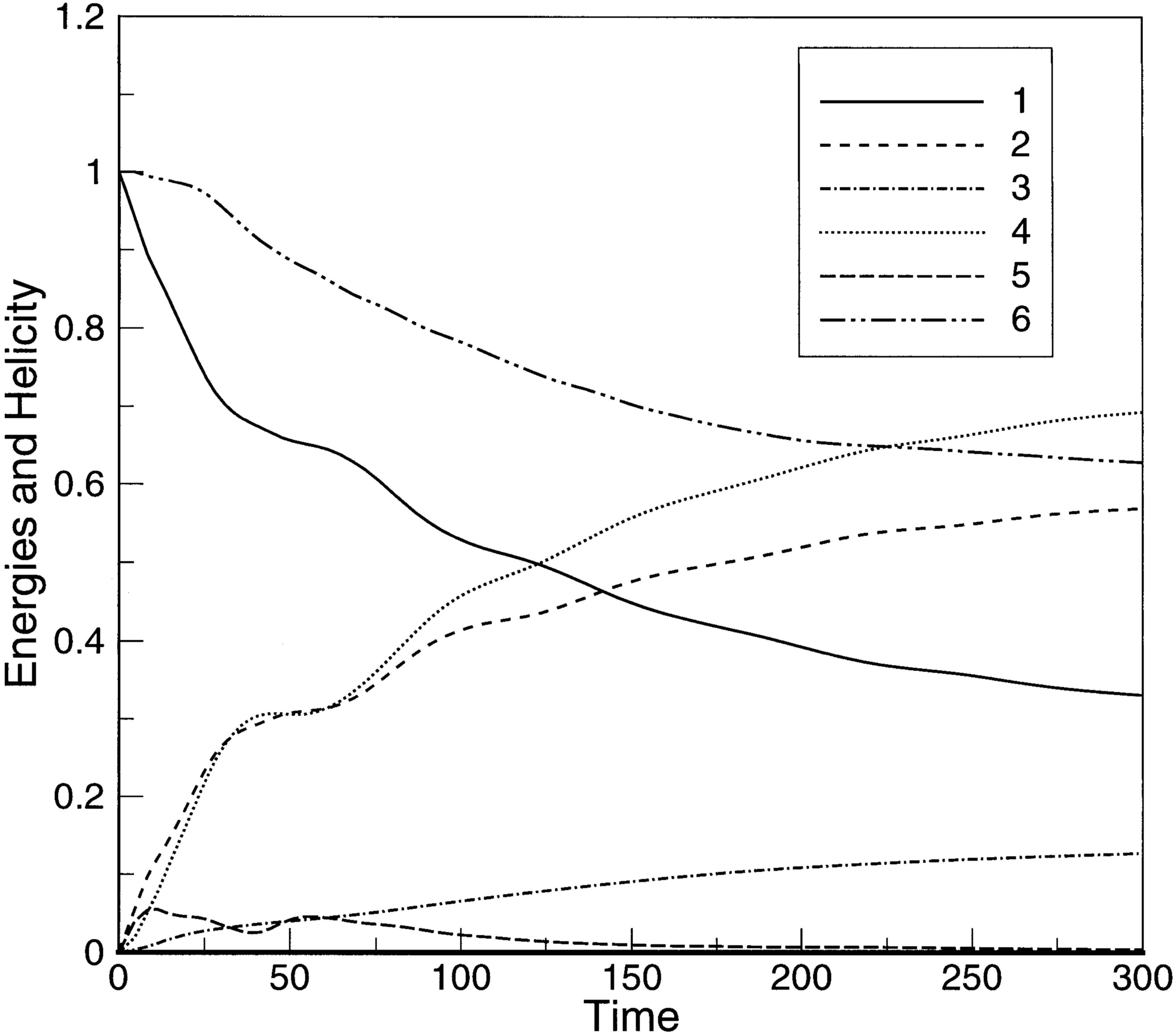
1.2
1
0.8
0.6
0.4
0.2
0
Energies and Helicity
0
50
100
150
200
250
300
Time
1
2
3
4
5
6

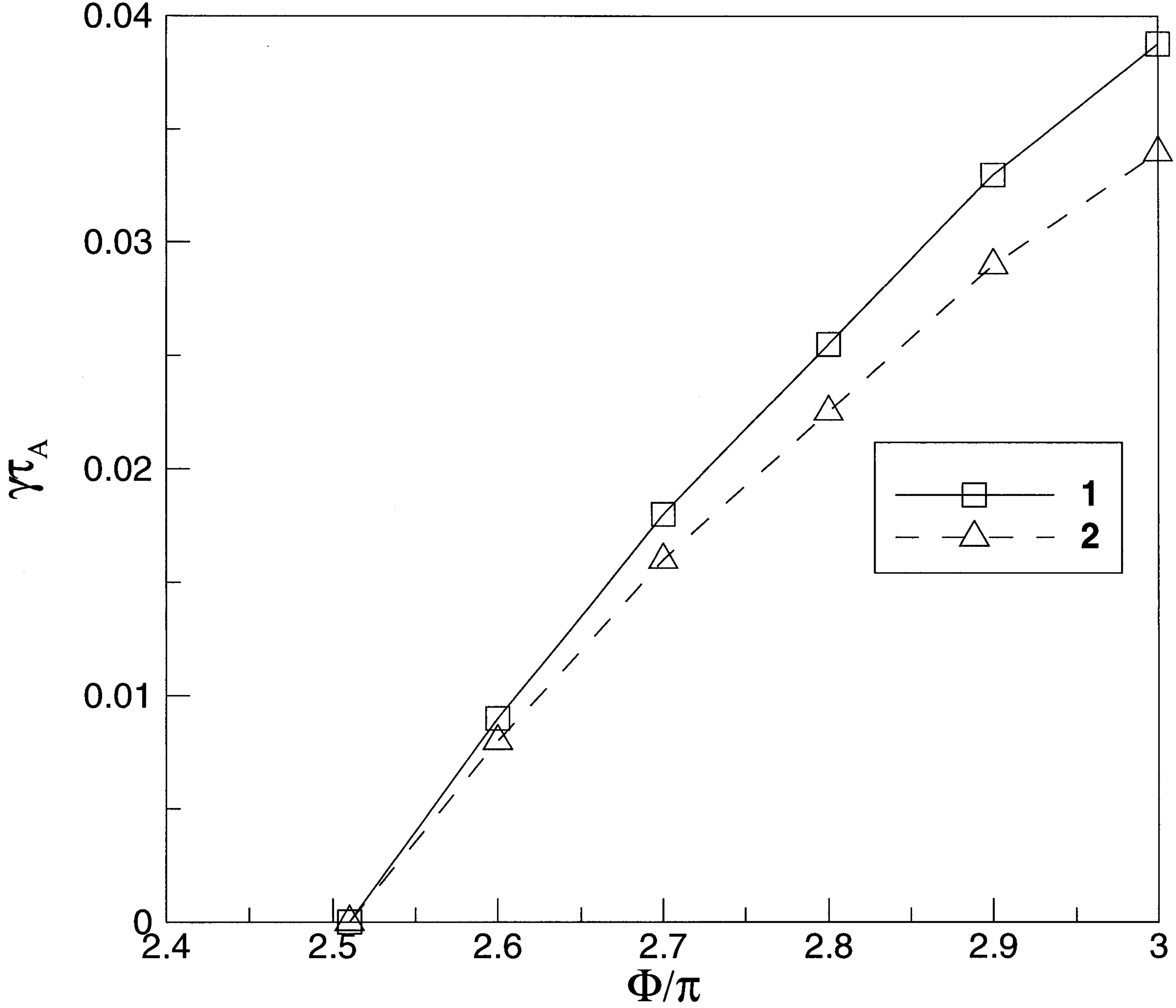
0.04
0.03
0.02
0.01
0
$\gamma\tau_A$
2.4
2.5
2.6
2.7
2.8
2.9
3
Φ/π
1
2

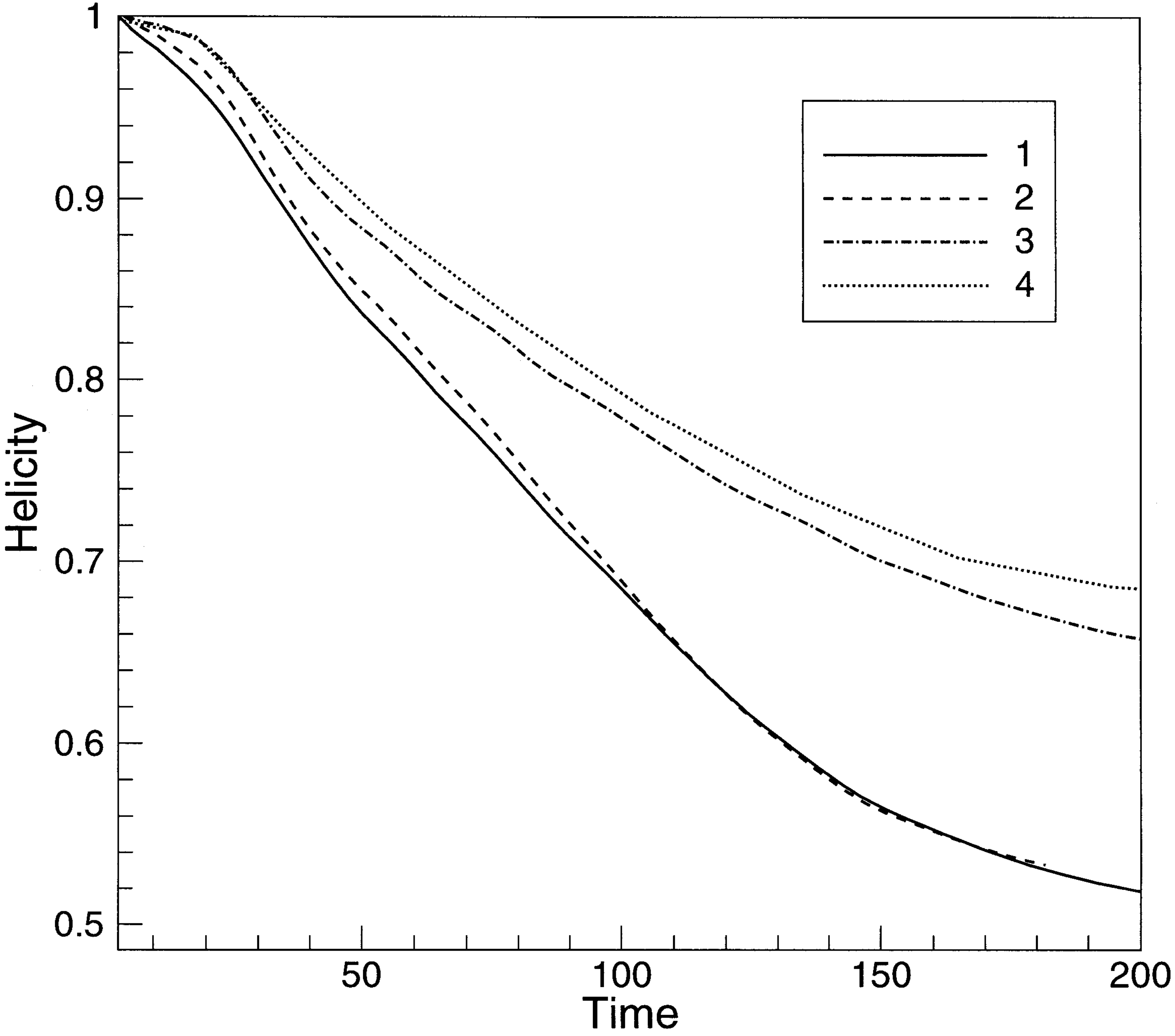

1
0.9
0.8
0.7
0.6
0.5
Helicity
50
100
150
200
Time
1
2
3
4